

Targeting IRE1 α reprograms the tumor microenvironment and enhances anti-tumor immunity in prostate cancer

Received: 20 July 2023

Accepted: 30 September 2024

Published online: 15 October 2024

 Check for updates

Bilal Unal^{1,2}, Omer Faruk Kuzu^{1,2}, Yang Jin¹, Daniel Osorio³, Wanja Kildal ², Manohar Pradhan², Sonia H. Y. Kung ⁴, Htoo Zarni Oo ⁴, Mads Daugaard ⁴, Mikkel Vendelbo⁵, John B. Patterson⁶, Martin Kristian Thomsen ⁷, Marieke Lydia Kuijjer ^{3,8,9} & Fahri Saatcioglu ^{1,2} 


Unfolded protein response (UPR) is a central stress response pathway that is hijacked by tumor cells for their survival. Here, we find that IRE1 α signaling, one of the canonical UPR arms, is increased in prostate cancer (PCa) patient tumors. Genetic or small molecule inhibition of IRE1 α in syngeneic mouse PCa models and an orthotopic model decreases tumor growth. IRE1 α ablation in cancer cells potentiates interferon responses and activates immune system related pathways in the tumor microenvironment (TME). Single-cell RNA-sequencing analysis reveals that targeting IRE1 α in cancer cells reduces tumor-associated macrophage abundance. Consistently, the small molecule IRE1 α inhibitor MKC8866, currently in clinical trials, reprograms the TME and enhances anti-PD-1 therapy. Our findings show that IRE1 α signaling not only promotes cancer cell growth and survival but also interferes with anti-tumor immunity in the TME. Thus, targeting IRE1 α can be a promising approach for improving anti-PD-1 immunotherapy in PCa.

The endoplasmic reticulum (ER) is the largest organelle in the cell. It is the major site for proper protein folding, processing and trafficking of membrane-bound and secreted proteins. In addition, ER is the major site for Ca²⁺ storage and functions as a stress sensor responding to increased demand for protein production and folding under both physiological and pathological conditions. ER stress initiates a series of coping mechanisms that are termed the unfolded protein response (UPR), which restructures the cellular transcriptional, translational, and degradation pathways to help resolve the defects in protein folding^{1,2}. This is achieved through the activation of three transmembrane ER proteins: inositol requiring enzyme 1 alpha (IRE1 α),

protein kinase RNA-dependent-like ER kinase (PERK) and activating transcription factor 6 (ATF6).

IRE1 α is both a protein kinase and an atypical site-specific RNase. Upon activation, IRE1 α RNase function activates the translation of transcription factor X-box protein 1 spliced (XBPIs) by removing an intron from the XBPI mRNA; in addition, it depletes select mRNAs through the process of regulated IRE1 α -dependent decay (RIDD)^{1,2}. XBPIs is involved in gene expression that supports ER-mediated protein folding, as well as ER-associated degradation (ERAD) of misfolded proteins, whereas RIDD depletes specific ER-targeted mRNAs to relieve the load on ER, as well as proteins involved in other processes in the cell.

¹Department of Biosciences, University of Oslo, Oslo, Norway. ²Institute for Cancer Genetics and Informatics, Oslo University Hospital, Oslo, Norway. ³Center for Molecular Medicine Norway, Nordic EMBL Partnership, University of Oslo, Oslo, Norway. ⁴Vancouver Prostate Centre, Department of Urologic Sciences, University of British Columbia, Vancouver, Canada. ⁵Department of Nuclear Medicine & PET Centre, Aarhus University Hospital, Aarhus, Denmark. ⁶Orinove Inc., Newbury Park, California, USA. ⁷Department of Biomedicine, Aarhus University, Aarhus, Denmark. ⁸Department of Pathology, Leiden University Medical Center, Leiden, the Netherlands. ⁹Leiden Center for Computational Oncology, Leiden University Medical Center, Leiden, the Netherlands.

 e-mail: fahris@uio.no

Recent studies have implicated IRE1 α -XBPs pathway deregulation in a number of pathological conditions, including metabolic disease, neurodegenerative disease, and cancer^{1–3}. We have previously found that IRE1 α -XBPs signaling is significantly increased in prostate cancer (PCa)^{4,5}. Consistently, genetic or small molecule targeting of IRE1 α resulted in significant inhibition of PCa tumor growth in multiple xenograft models in immunodeficient mice. We have shown that this was due, at least in part, to the inhibition of c-MYC expression driven by IRE1 α -XBPs signaling⁵.

IRE1 α -XBPs signaling has also been implicated in immune cell function (for a review, see ref. 6). In bone-marrow-derived macrophages, Toll-like receptor 2 (TLR2) and TLR4 activated IRE1 α -XBPs signaling to enable production and secretion of cytokines, such as tumor necrosis factor (TNF), interleukin 1 beta (IL-1 β) and IL-6⁷. In TLR8-activated mouse bone marrow-derived dendritic cells (BMDCs), IRE1 α -XBPs signaling increased IL-23 expression upon palmitate exposure⁸. In dendritic cells (DCs), macrophages and neutrophils that are exposed to ER stress or stimulated by plasma membrane-bound TLRs, IRE1 α -XBPs signaling was necessary for normal eicosanoid metabolism and production of the pain-causing lipid mediator prostaglandin E2 (PGE2)⁹. In natural killer (NK) cells, IRE1 α -XBPs signaling was required for response to viral infection and tumors¹⁰.

In addition to these and other roles of the IRE1 α -XBPs pathway in normal immune function, recent studies have demonstrated that it is also involved in antitumor immunity via altering the function of myeloid cells, T cells, and NK cells in the tumor microenvironment (TME) (for a review, see ref. 10). For example, IRE1 α -XBPs signaling was found to be essential for proliferation of NK cells in mouse melanoma models¹¹. In metastatic ovarian cancer mouse models, there is sustained IRE1 α -XBPs activation in tumor-associated DCs driving triglyceride biosynthesis and lipid droplet formation, resulting in the loss of their antigen-presenting capacity¹². Similarly, T cells isolated from human ovarian cancer specimens, either solid tumors or ascites fluid, had increased IRE1 α -XBPs pathway activity, and this was linked to decreased intratumoral T cell infiltration and reduced interferon- γ (IFN- γ) expression¹³. These findings suggest that inhibiting the IRE1 α -XBPs pathway may improve the efficacy of immune checkpoint blockade (ICB) and adoptive T cell immunotherapies in solid tumors that are refractory to these approaches.

Here, we study the potential effects of IRE1 α signaling on the PCa TME in multiple syngeneic mouse models as well as in an orthotopic model. We demonstrate that IRE1 α signaling in cancer cells reshapes the TME and pharmacological targeting of IRE1 α can enhance the response to anti-PD-1 blockade therapy. These findings have clinical implications for treating immunologically ‘cold’ PCa.

Results

IRE1 α is upregulated in human PCa specimens

We have previously shown that androgens, which activate a major signaling pathway implicated in PCa progression, modulate IRE1 α -XBPs branch of the UPR⁴. Consistently, inhibition of IRE1 α RNase activity or knockdown of XBPs strongly interfered with PCa in multiple preclinical models⁵. To further delineate the role of IRE1 α in PCa, we first assessed IRE1 α expression in human PCa specimens compared with normal prostate using immunohistochemistry (IHC). IRE1 α expression was significantly increased in PCa samples compared to normal prostate tissue and correlated with a higher Gleason score (Fig. 1A–C), suggesting that it may have prognostic significance. This observation was further confirmed in an independent PCa cohort where IRE1 α expression was also significantly increased in PCa samples compared to adjacent normal tissues (Fig. 1D). In addition, in the Cancer Genome Atlas (TCGA) dataset, IRE1 α mRNA expression is highly correlated with androgen receptor (AR) mRNA and protein levels (Supplementary Fig. 1A, B). This was consistent with the IHC data where there were increased nuclear AR levels with

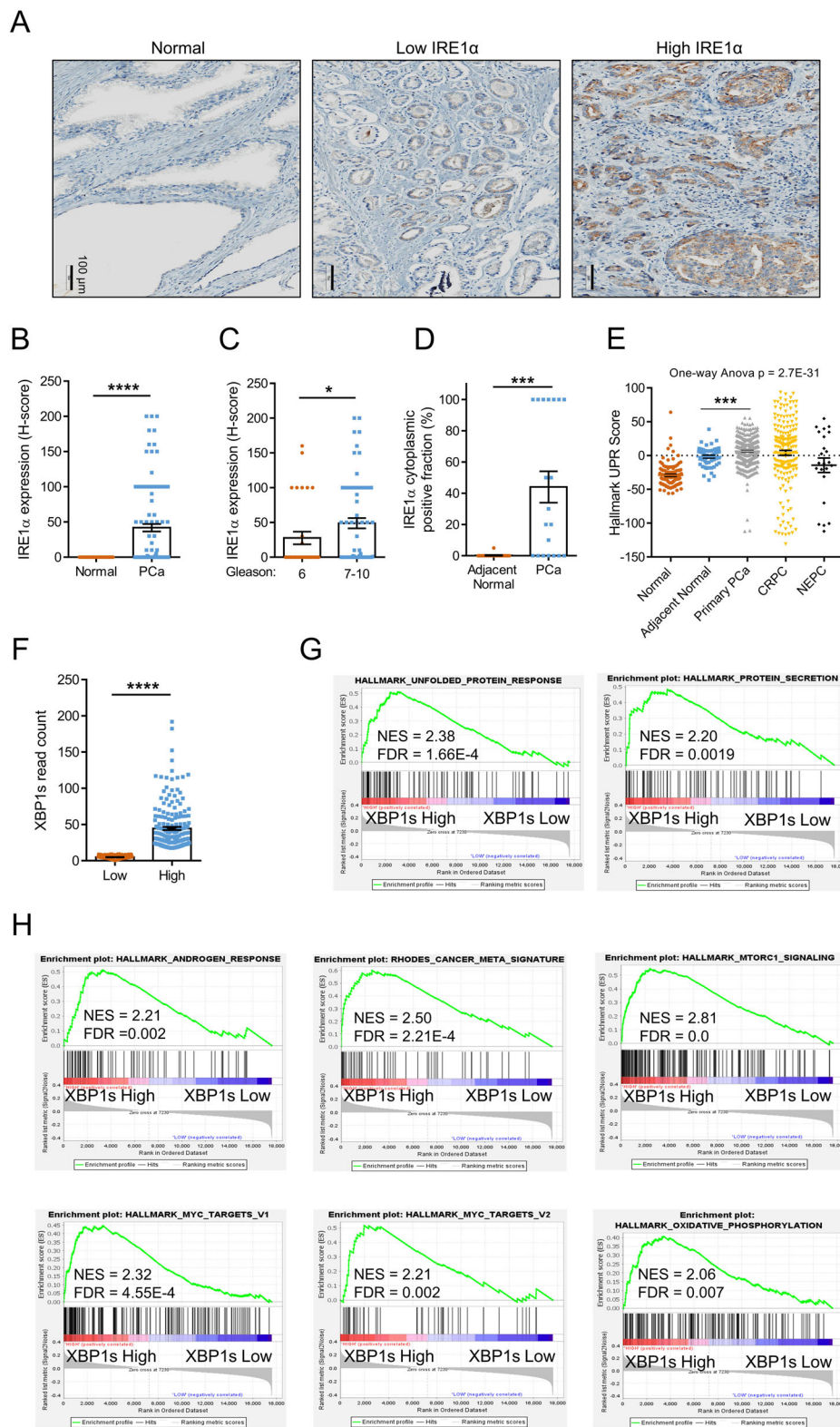
increasing IRE1 α expression (Supplementary Fig. 1C, D). Further analysis of the TCGA dataset, particularly the RPPA (Reverse Phase Protein Array) data, suggests that the phosphorylation levels of AKT, mTOR, and ERK are associated with increased IRE1 α mRNA expression (Supplementary Fig. 1E, F). In addition, IRE1 α mRNA levels correlated with the hypoxia-inducible factor 1 subunit alpha (HIF1A) mRNA expression (Supplementary Fig. 1G), suggesting that there may be an interplay between IRE1 α signaling and cellular hypoxic responses in PCa.

Given the central role of IRE1 α in UPR signaling, we next evaluated UPR activity across different PCa disease stages using the hallmark UPR gene signature in publicly available datasets¹⁴. In contrast to normal prostate samples, the UPR score was significantly increased in both tumor-adjacent normal samples and primary PCa; furthermore, primary PCa samples displayed higher scores than tumor-adjacent normal samples, suggesting the induction of UPR in the TME (Fig. 1E). To further explore whether this difference in UPR signature expression involves the IRE1 α -XBPs branch of UPR, we determined XBPs mRNA levels in the TCGA PCa dataset¹⁵ by dividing the patients according to XBPs levels (top and bottom 40% expression) (Fig. 1F). Gene set enrichment analysis (GSEA) showed that genes regulating hallmark UPR and protein secretion were downregulated in patients with low XBPs read counts, as expected (Fig. 1G). Consistent with our previous findings⁵, PCa patient tumors exhibiting high XBPs mRNA levels showed increased expression of genes that regulate hallmarks of cancer growth such as androgen response, cancer progression and transformation, mTORC1 signaling, oxidative phosphorylation and MYC targets (Fig. 1H). These findings further demonstrate the significance of IRE1 α -XBPs signaling in PCa.

Tumor-intrinsic IRE1 α loss may influence anti-tumor immunity in the PCa TME

Activation of the IRE1 α -XBPs branch of the UPR has been associated with cancer growth and malignancy¹⁶. However, the impact of IRE1 α activation in cancer cells on anti-tumor immune responses remains largely unknown. To investigate this possibility, we used the Myc-CaP syngeneic mouse PCa model, derived from a transgenic mouse strain in which human c-MYC oncoprotein expression is specifically targeted to the prostate^{17,18}. We first generated IRE1 α knock-out (KO) Myc-CaP cell lines using CRISPR-Cas9 mediated genome editing (Supplementary Fig. 2A, B). Interestingly, IRE1 α KO Myc-CaP cells did not display any changes in cell viability and growth in vitro either at basal levels (Supplementary Fig. 2C, D) or upon treatment with the UPR activator thapsigargin (TG) (Supplementary Fig. 2E); this is in contrast to its key roles in cancer, including PCa (for reviews, see refs. 16,19). In addition, genetic or pharmacological targeting of IRE1 α in Myc-CaP cells in vitro did not markedly affect apoptosis, either in the absence or presence of TG (Supplementary Fig. 2F–H). Furthermore, the cell cycle was not consistently affected by the absence of IRE1 α , although two of the three clones showed slight increases in G2 phase (Supplementary Fig. 2I).

To gain insight into the global transcriptomic changes upon loss of IRE1 α , we performed RNA-seq, which revealed a strong correlation ($r > 0.56$) among the three different IRE1 α KO clones, suggesting a high degree of similarity in their gene expression profiles (Supplementary Fig. 3A). Analysis of significantly deregulated genes identified 240 genes that were consistently downregulated across all three independent IRE1 α KO clones (Supplementary Fig. 3B) (Supplementary Data 1). As expected, GSEA of these genes demonstrated enrichment of UPR and UPR-related pathways, including IRE1 α -activated chaperones, protein processing in the ER, and asparagine N-linked glycosylation (Supplementary Fig. 3C). In addition, hallmark UPR gene expression was significantly downregulated in IRE1 α KO cells (Supplementary Fig. 3D). These data are consistent with known pathway connections of IRE1 α signaling^{1,2}.



We next investigated the functional role of IRE1α-XBP1s signaling in the PCa TME. To explore the tumor cell-intrinsic effect of IRE1α activation on PCa tumor growth, we injected the IRE1α WT and the three KO clones of Myc-CaP cells into FVB mice and monitored tumor growth. Loss of IRE1α dramatically reduced tumor growth (Fig. 2A, B). Consistent with these results, the growth of IRE1α KO Myc-CaP tumors was significantly hindered in the orthotopic setting compared to wild type Myc-CaP tumors (Supplementary Fig. 3E, F). To evaluate whether

the reduction in tumor growth was attributable to the IRE1α-XBP1s signaling axis, we ectopically expressed XBP1s in Myc-CaP IRE1α KO #1 cells, which showed the greatest reduction in tumor growth. XBP1s overexpression in IRE1α KO cells rescued the expression of IRE1α-XBP1s target genes (Edem1, p58IPK, and Pdia6) in vitro indicating its functionality (Supplementary Fig. 3G). Importantly, ectopic XBP1s expression rescued the growth of IRE1α KO tumors in vivo (Supplementary Fig. 3H).

Fig. 1 | IRE1 α signaling is activated in human PCa. **A** IRE1 α expression was examined by IHC in normal prostate ($n = 22$) and PCa samples ($n = 117$); representative images, including low ($n = 66$) and high ($n = 51$) IRE1 α expression are shown. Images are presented from Vancouver cohort. **B** IHC quantification from A. **C** IRE1 α expression scores from B were stratified according to Gleason scores [Gleason 6 ($n = 31$) and 7–10 ($n = 65$)] as indicated. Among the 64 grade 7 to 10 tumor samples analyzed, approximately 47% (30 samples) exhibited high IRE1 α expression (H-score > 5). **D** IRE1 α IHC analysis results from the Oslo cohort ($n = 20$) matched to adjacent normal tissue ($n = 20$). **E** UPR gene expression is dysregulated in PCa. Hallmark UPR gene expression score in primary ($n = 499$), castration resistant PCa (CRPC) ($n = 183$), or neuroendocrine PCa (NEPC) ($n = 23$) samples

compared with normal prostate tissue from the GTEx ($n = 119$) or tumor adjacent normal TCGA ($n = 52$) datasets. Data analyzed by One-way Anova. **F** TCGA PCa samples were split into two groups as low ($N = 200$) or high ($N = 200$) based on normalized XBPIs splicing read counts and used in GSEA and immune cell infiltration analyzes. **G** GSEA plots for Hallmark UPR and protein secretion in the TCGA PCa dataset, where samples were split based on XBPIs read counts. **H** As in G, but different Hallmarks are interrogated. Mean \pm standard error by unpaired two-tailed Mann Whitney t-test is presented for figure (**B**, **C**, **C** ($p = 0.0235$), **E** ($p = 0.0001$), and **F**; two-tailed paired Wilcoxon signed-rank test was used for **D** ($p = 0.0002$). * $p < 0.05$, *** $p < 0.001$, **** $p < 0.0001$.

To evaluate whether the decreases in IRE1 α KO Myc-CaP tumor growth were due to protective anti-tumor immunity, we conducted a xenograft experiment in nude mice that had a greatly reduced number of T lymphocytes. As opposed to dramatic regression in tumor growth observed in immunocompetent FVB mice, loss of IRE1 α in Myc-CaP cells in nude mice only mildly affected tumor growth at later time points (Fig. 2C). These data suggest that anti-tumor immunity may play a role in mediating the IRE1 α effects in tumor growth in FVB mice.

To explore the potential mechanisms of tumor regression upon IRE1 α targeting, we performed RNA-seq from IRE1 α WT and the three independent KO tumors. GSEA on the RNA-seq data confirmed the downregulation of UPR target genes (Supplementary Fig. 4A) and classical IRE1 α target pathways, such as the expression of chaperones and proteins involved in N-linked glycosylation (Fig. 2D) (Supplementary Data 1). Consistent with human PCa patient tumors that exhibit low XBPIs and IRE1 α mRNA levels (Fig. 1H and Supplementary Fig. 1E–G), there was downregulation of genes that control hallmarks of cancer growth in IRE1 α KO tumors such as hypoxia, oxidative phosphorylation, and mTORC1 signaling (Supplementary Fig. 4B–E). Interestingly, the loss of IRE1 α also significantly increased immune-related gene expression in the tumors (Fig. 2E). Among the top enriched pathways for upregulated genes were IFN response-related pathways followed by various aspects of immune function, such as innate and adaptive immunity, T and NK cell-mediated immunity and their activation (Fig. 2E–G). Altogether, these results indicated that IRE1 α -XBPIs signaling in cancer cells may alter protective immunity in the PCa TME.

IRE1 α loss in cancer cells augments IFN- γ signaling response in the PCa TME

It is noteworthy that while hallmark UPR genes were downregulated in IRE1 α -deficient tumors, there was a significant increase in the expression of the genes involved in IFN- α or - γ transcriptional responses (Fig. 3A, B). The roles of IFN- γ in anti-tumor immune responses, particularly in the context of T and NK cell-mediated immunity, as well as antigen presentation, are well established^{20,21}. Although IFN- γ transcriptional response genes were upregulated in IRE1 α KO tumors in vivo, their expression was not changed in KO cells in vitro (Fig. 3C). Altered expression of ER stress and IFN- γ response genes in IRE1 KO tumors were validated by qPCR analysis (Fig. 3D).

To obtain additional insight into the characteristics of Myc-CaP tumor TME upon IRE1 α loss, we performed proteomics analysis on tumor samples from IRE1 α KO clones #2 and #3 (no tumor material was left for this analysis for clone #1). We detected 6505 proteins in IRE1 α WT and KO tumors (Supplementary Data 2). Among these, 202 were upregulated and 378 were downregulated (absolute fold-change ≥ 1.2 and $p < 0.05$, WT vs KO) (Supplementary Data 2). Analysis of these data revealed that proteins modulating the immune system, complement system, and notably IFN- α and - γ responses, were significantly upregulated and enriched in the TME upon loss of IRE1 α (Fig. 3E, F). In contrast, proteins regulating hallmarks of cancer growth and survival, such as UPR, mTORC1 signaling, MYC targets, glycolysis, oxidative phosphorylation, and hypoxia were all significantly enriched among

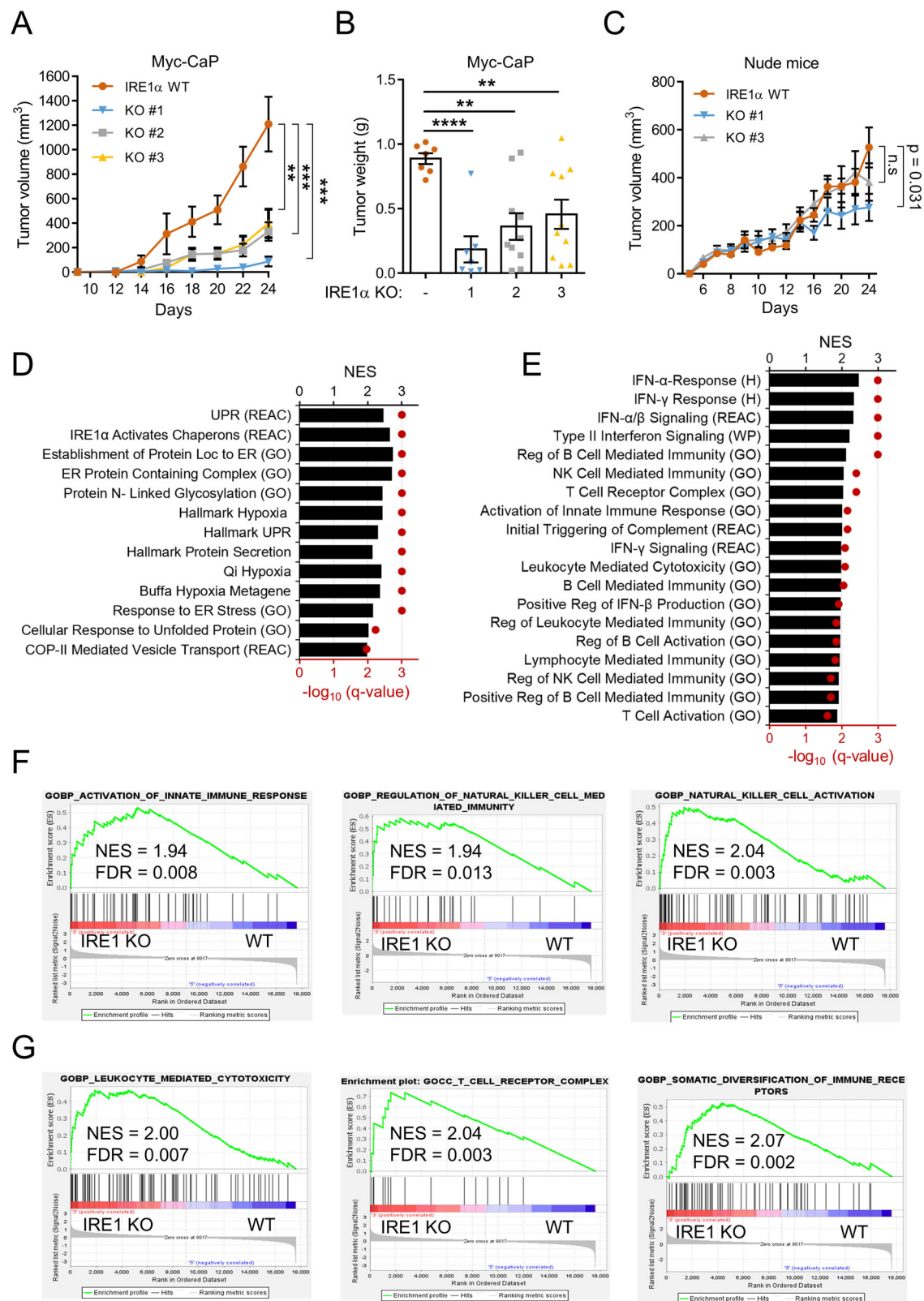
the downregulated proteins in IRE1 α KO tumors, consistent with the RNA-seq data (Fig. 3F and Supplementary Fig. 4). Coordinate analysis of differentially regulated genes from both RNA-seq and proteomics data revealed 182 upregulated and 192 downregulated common genes (Fig. 3G and Supplementary Data 2) that displayed significant changes for IFN- γ response (e.g. HELZ2, ZBP1, PML, etc.) and UPR target gene expression (e.g. DNAJC3, MTHFD2, PDIA6, etc.), respectively (Fig. 3H). These findings suggest that loss of IRE1 α in Myc-CaP cells enhances the IFN transcriptional response within the TME, which is essential for anti-tumor immunity.

Loss of IRE1 α in cancer cells reprograms the PCa TME landscape

To explore the molecular and cellular mechanisms that underlie the enhanced IFN response in IRE1 α KO tumors, we conducted a new experiment where WT and IRE1 α KO Myc-CaP tumors were subjected to single-cell RNA-sequencing (scRNA-seq). Consistent with previous data (Fig. 2), the loss of IRE1 α led to significant tumor regression in FVB immunocompetent mice (Supplementary Fig. 5A, B). Furthermore, loss of IRE1 α in cancer cells resulted in significantly extended survival of tumor-bearing mice (Supplementary Fig. 5C). After quality filtering, we obtained data from 11071 and 8434 single cells from WT and IRE1 α KO tumors, respectively. Upon scRNA-seq clustering analysis, we annotated 8 distinct cell type clusters in addition to the tumor cells (Fig. 4A–C and Supplementary Fig. 5D). In contrast to WT Myc-CaP tumors, the abundance of pericytes, tumor-associated macrophages (TAMs), and cancer associated fibroblasts (CAFs) were markedly reduced (50–75%) in IRE1 α KO tumors. Sub-clustering of NK Cells + T Cells revealed three different T cell subtypes in addition to NK cells subtypes (Supplementary Fig. 5E). Interestingly, the abundance of immunosuppressive regulatory T cells (Tregs) (expressing Foxp3, Ctla4 and Pd-1) were markedly reduced in IRE1 α KO tumors (Fig. 4C and Supplementary Fig. 5E). There was also a slight increase in the abundance of CD8+ T cells, while we observed a marked increase in NK cells (Fig. 4C).

Among the different cell types in the TME other than cancer cells, TAMs were the most abundant cell type that constituted around 9% of the tumors. Sub-clustering of TAMs revealed five different clusters expressing distinct gene markers (Fig. 4D and Supplementary Fig. 6A). Based on the marker gene expression profile reported in a recently published study²², we annotated four clusters as Regulatory TAMs (Reg-TAMs), Inflammatory TAMs (Inflam-TAMs), Proliferating TAMs (Prolif-TAMs), and IFN primed monocytes/macrophages (IFN-Mo/M ϕ). The fifth cluster, which showed expression of cancer cell markers (likely due to doublets), was subsequently omitted from further analysis. Reg-TAMs constituted the main TAM subtype accounting for approximately 40% of all TAMs in WT tumor samples (Fig. 4E). Similar to the other TAM subtypes, their abundance was markedly decreased in IRE1 α KO tumors (Fig. 4E).

To investigate the origin of the augmented IFN response observed in the TME of IRE1 α KO tumors, we conducted GSEA on each specific cell type annotated within the scRNA-seq data. Genes associated with IFN- α and - γ responses were significantly enriched in all identified TAM subtypes, as well as in cancer cells and dendritic cells (DCs) (Fig. 4F).



There were no significant differences in IFN- α and - γ responses in other cell types (Supplementary Fig. 6B). On the other hand, genes responsible for protein secretion were significantly enriched among down-regulated in IRE1 α KO cancer cells, consistent with the proteomics and total RNA-seq data presented earlier (Figs. 2D and 3F). Taken together, these results indicate that the activation of IRE1 α signaling in cancer cells could remodel the TME.

A small molecule inhibitor of IRE1 α inhibits tumor growth in syngeneic PCa mouse models

To assess whether pharmacological inhibition of IRE1 α could inhibit PCa growth in a syngeneic setting, we first tested the effect of IRE1 α RNase inhibitor MKC8866 on Myc-CaP tumors. Myc-CaP cells were injected into FVB mice, which were either left untreated or treated with MKC8866, and tumor growth was monitored (Fig. 5A).

Fig. 2 | Loss of IRE1 α inhibits PCa tumor growth and activates the expression of anti-tumor immunity-related genes in the TME. A, B Myc-CaP IRE1 α KO cell lines were generated by CRISPR-Cas9 genome editing. Cells were subcutaneously injected into two flanks of FVB mice. **A** Tumor sizes were measured at the indicated time points for WT ($n = 4$ mice, 7 tumors) and three independent IRE1 α KO clones - KO1 ($n = 4$ mice, 7 tumors), KO2 ($n = 5$ mice, 10 tumors) and KO3 ($n = 5$ mice, 10 tumors). **B** Same as in (A) but tumor weights were measured at the end of the experiment. **C** IRE1 α WT ($n = 3$ mice, 5 tumors) or KO clones 1-3 ($n = 3$ mice, 6 tumors per KO clone) of Myc-CaP cells grown as xenografts in nude mice. **D, E** Tumor samples were collected at the end of the experiment presented in Fig. 2A, RNA was isolated and subjected to RNA-seq analysis. KO clones ($n = 3$ mice, 3

tumors per KO clone) were compared with WT ($n = 4$ mice, 4 tumors) samples. GSEA for (D) downregulated or (E) upregulated genes in IRE1 α KO tumors is presented. Note that for several processes, the q -value equals 3; this is because the GSEA tool computes 3 as the maximum possible q -value. **F, G** Enrichment plots for the indicated datasets enriched in GSEA analysis related to (F) innate or (G) adaptive immunity are presented. Mean \pm standard error for two-tailed student's t -test is presented for Figure (A) (IRE1 α WT vs KO #1 ($p = 0.0008$), vs KO #2 ($p = 0.0007$), vs KO #3 ($p = 0.003$), for Figure (B) (IRE1 α WT vs KO #1 ($p = 3.4E-05$), KO #2 ($p = 0.001$), vs KO #3 ($p = 0.008$), and for Figure C (WT vs KO #3, $p = 0.87$); ** $p < 0.01$, *** $p < 0.001$, n.s., non-significant.

MKC8866 treatment dramatically reduced Myc-CaP tumor growth (Fig. 5B, C).

To model advanced PCa, which commonly involves MYC amplification and PTEN loss in patient tumors²³⁻²⁵, we generated a PTEN KO Myc-CaP cell line by CRISPR-Cas9 genome editing. As expected, the loss of PTEN dramatically accelerated tumor growth in vivo (Fig. 5D, E). Moreover, the expression of immune checkpoint ligands PD-L1 and B7-H3 was increased in PTEN KO cells (Fig. 5F), consistent with previous studies^{26,27}. Notably, the expression of these ligands was correlated with higher IRE1 α mRNA expression in the TCGA PCa dataset (Fig. 5G). In this model, MKC8866 also effectively suppressed tumor growth, demonstrating its potential translational relevance in advanced PCa as well (Fig. 5H, I, and K).

To further validate our results, we employed RM-1 cells as another syngeneic mouse PCa model, which expresses Ras and Myc oncogenes²⁸. Although, RM-1 tumors grew even faster than Myc-CaP PTEN KO tumors, MKC8866 was also effective in inhibiting their growth (Fig. 5H, J, and L). Taken together, these findings demonstrate that inhibition of IRE1 α signaling by MKC8866 significantly reduces tumor growth across various syngeneic PCa mouse models, highlighting its translational potential as an effective therapeutic option for PCa.

MKC8866 synergizes with anti-PD-1 immune checkpoint blockade therapy

Cancer immunotherapy has recently revolutionized therapeutic approaches for various cancer types. For example, immune checkpoint inhibitors have been highly successful in patients with metastatic melanoma, renal cell carcinoma, head and neck cancer, and non-small cell lung cancer²⁹; however, these therapies have thus far failed to provide significant clinical benefit for PCa³⁰⁻³³. Given the significant effect of MKC8866 and activation of the immune microenvironment as exemplified by the augmented IFN response in IRE1 α KO Myc-CaP tumors, we investigated whether MKC8866 could increase responsiveness to anti-PD-1 therapy. We treated Myc-CaP tumor-bearing mice either with MKC8866 (at a suboptimal dose) alone, an anti-PD-1 antibody alone, or their combination (Fig. 6A). Treatment with either MKC8866 or the anti-PD-1 antibody alone modestly impaired tumor growth, whereas the combination therapy led to a dramatic inhibition of tumor growth (Fig. 6B, C).

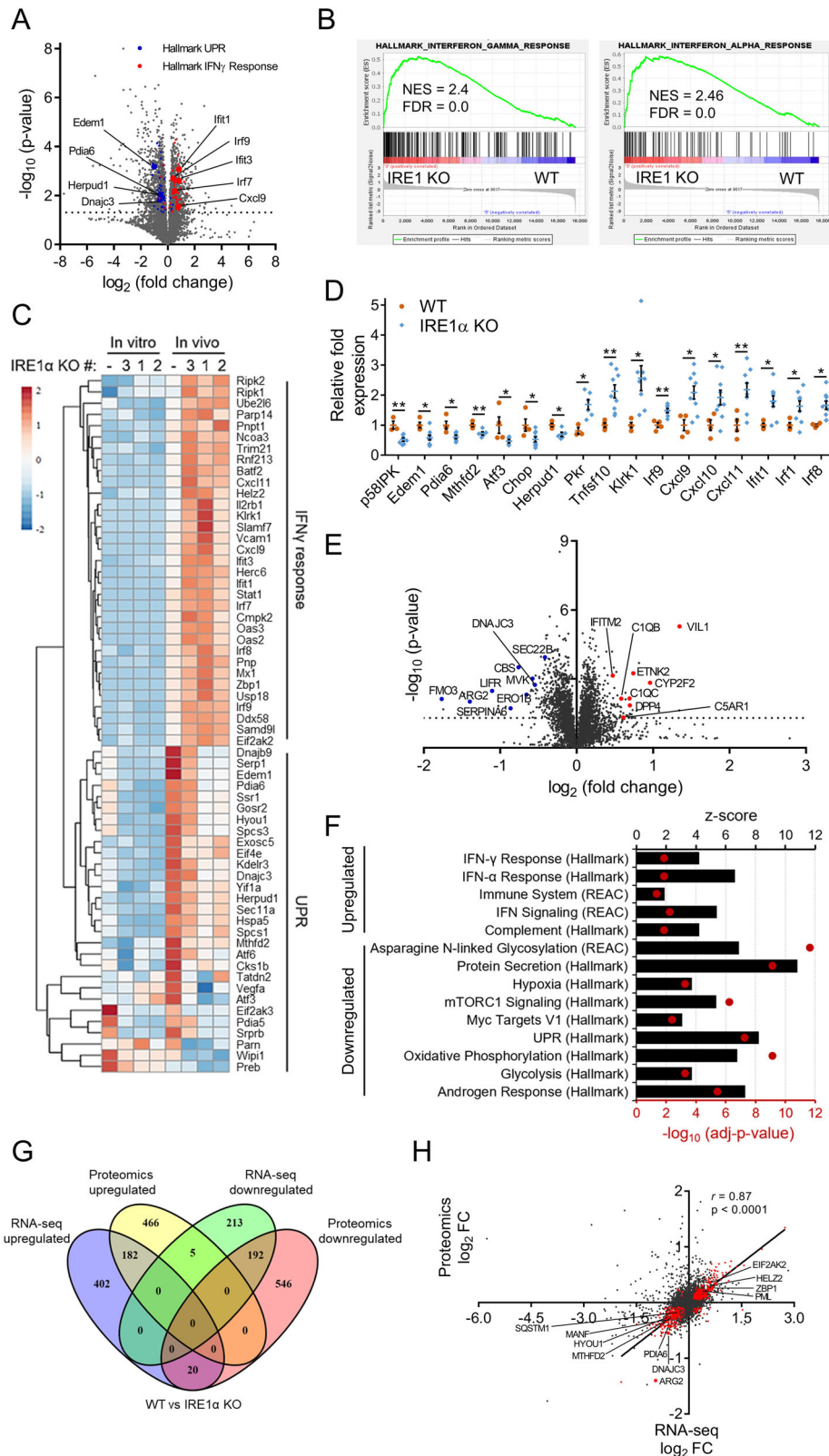
We repeated this experiment in the Myc-CaP PTEN KO model and observed similar results (Fig. 6D-F). In the RM-1 model, MKC8866 modestly inhibited tumor growth, whereas the anti-PD-1 antibody treatment had no significant effect; in contrast, the combination therapy exhibited significantly greater efficacy than MKC8866 treatment alone (Fig. 6G-I). In all PCa mouse models tested, no significant changes in the body weight of mice were observed across the three different mouse models (Fig. 6J), suggesting that treatments did not cause any apparent toxicity. Taken together, these data suggest that IRE1 α inhibition can enhance the therapeutic efficacy of anti-PD-1-based ICB in PCa.

Combination therapy modulates TAMs and boosts infiltration of CD8+ T and NK cells into the TME

To date, ICB therapy has largely failed as a potential treatment option in PCa, except for partial responses in the minority of patients whose tumors have high mutational burden^{34,35}. This has prompted significant efforts to discover the underlying reasons for this resistance and to develop therapeutic approaches to sensitize PCa to ICB therapy. To explore the mechanisms that underlie the significant therapeutic responses induced by MKC8866 + anti-PD-1 combination therapy, we performed scRNA-seq on tumors from the Myc-CaP PTEN KO experiment described in Fig. 6D-F. We observed notable changes in various cell populations under different treatment conditions (Fig. 7A, B, and Supplementary Fig. 7A). Treatment with either MKC8866 or anti-PD-1 alone resulted in a marked increase in the abundance of CD8+ T cells and NK cells (Fig. 7B). Remarkably, combination therapy further boosted the representation of these cells in the TME (Fig. 7B). Analysis of differentially expressed genes in the CD8+ T cell cluster revealed that combination therapy increased the expression of T cell activation markers such as *Gzmb*, *Prfl*, and *Nkg7* (Fig. 7C). Expression of *Ccl5*, a T cell activation marker and chemoattractant for T and NK cells³⁶, increased more than 32-fold in CD8+ T cells upon combination therapy compared to control tumors (Fig. 7C). These findings underscore the potential of MKC8866 + anti-PD-1 combination therapy to enhance immune cell infiltration and activation within the TME.

In Myc-CaP IRE1 α KO tumors there was significantly increased expression of IFN response genes, especially in TAMs and dendritic cells (Figs. 3 and 4); we therefore investigated whether MKC8866 also augments the IFN response in the TME. GSEA indicated that MKC8866 or anti-PD-1 treatments induced the expression of genes involved in IFN- α and IFN- γ signaling response in select immune cell types, such as dendritic cells and some TAM subtypes, whereas combination treatment significantly upregulated both pathways, in almost all immune cell types (Fig. 7D). MKC8866 alone increased the abundance of certain TAM subtypes such as Reg-TAMs and IFN-Mo/M ϕ in the TME; however, the overall abundance of TAMs was reduced with combination therapy (Supplementary Fig. 7B, C). The exception was for IFN-Mo/M ϕ subset, which exhibited higher expression levels of MHC-II component genes (*H2-aa*, *H2-Eb1*, *H2-ab1*, and *Cd74*) (Supplementary Fig. 7D), characteristic of MI-like macrophages³⁷. Interestingly, the combination therapy shifted the transcriptional profile of all TAM subtypes towards an MI-like phenotype by upregulating the expression of genes involved in MHC-II components, IFN responses (*ligp1*, *Gbp2b*, and *Cxcl9*), and inflammatory response and activation (*AW112010*, *Nos2*, *Cd86*) (Fig. 7E and Supplementary Fig. 7E). However, the expression of genes associated with M2 macrophages such as *Cd63*, *Spp1*, *Lyz2*, and *Pf4* was downregulated in the TAMs upon combination therapy (Fig. 7E and Supplementary Fig. 7F).

In addition to these observations, there was significant increase in the expression of genes involved in antigen processing and presentation, such as *B2m*, *Cd74*, *Psmb8*, and *Psme2* in cancer cells upon combination therapy (Supplementary Fig. 7G). Interestingly, CellChat analysis of scRNA-seq data from combination therapy showed that the NK cells + T cells cluster has substantial interactions with other cell



types, such as cancer cells, macrophages, and dendritic cells, via the MHC-I signaling pathway (Fig. 7F). Taken together, these data suggest that combination therapy may enhance anti-tumor immunity by reprogramming TAMs to a more pro-inflammatory and antigen-presenting state.

Previous studies have shown that ICB resistance is associated with the upregulation of stress response genes HSPA1A and HSPA1B in

CD4⁺/CD8⁺ T cells across various cancer types^{35,38}. Interestingly, we found that combination therapy reduced the expression of both genes in CD8⁺ T cells (Fig. 7C and G). Furthermore, in these cells, combination therapy increased expression of T cell activation markers (Ccl5, Gzmb, Nkg7, and Prfl) and led to a transcriptional profile resembling the profile of CD8⁺ T cells from anti-PD-1 responsive patients with mCRPC³⁵ (Figs. 7G, H). These findings highlight the potential of

Fig. 3 | IRE1 α loss in cancer cells augments the IFN signaling response in PCA tumors. The RNA-seq data from Fig. 2 was analyzed in further detail. **A** Volcano plot indicating the up- and down-regulated genes in tumors from the three independent Myc-CaP IRE1 α KO clones (based on average gene expression); the most prominent gene sets, Hallmark UPR and IFN- γ response genes are color coded in blue and red, respectively. **B** GSEA plots show the enrichment of IFN- γ and IFN- α responses in IRE1 α KO vs WT comparison. **C** The heatmap displays genes differentially expressed in WT and IRE1 α KO (#1-3) tumor samples, as well as their expression in the RNA-seq data from in vitro grown cells. UPR and IFN- γ response genes are indicated. **D** Expression of specific genes from tumors of WT ($n = 4$ tumors, except for p58IPK and Pkr genes ($n = 3$ tumors), and IRE1 α KO clones ($n = 9$ tumors, except for genes Pdia6, Atf3, and Pkr ($n = 6$ tumors), Mthfd2 and Herpud1 ($n = 5$ tumors), p58IPK and Irf9 ($n = 7$ tumors), and Klrk4 ($n = 8$ tumors)) were analyzed by qRT-PCR

analysis. Source data and exact p -values are provided as a Source Data for this figure. **E, F** Tumor samples collected at the end of the experiment from Fig. 2A were analyzed by proteomics. **E** Volcano plot shows upregulated (red) and down-regulated (blue) proteins in IRE1 α KO tumors ($n = 3$ mice, 3 tumors) compared to WT ($n = 4$ mice, 4 tumors) counterparts. **F** Enrichr results of selected pathways for up- and down-regulated proteins are indicated. **G** RNA-seq and proteomics data were compared in a Venn diagram. **H** Scatter plot shows high correlation between proteomics and RNA-seq results for IRE1 α KO vs WT comparison. Genes with significantly altered expression ($p < 0.05$) in both experiments are indicated in red. Mean \pm standard error by two-tailed student's t -test is presented for figure (D). Two-tailed student's t -test is used for figure **A, E**, and **H**. Two-sided Fisher's exact test is used for figure **F**. * $p < 0.05$, ** $p < 0.01$. r represents Spearman correlation where indicated.

MKC8866 + ICB combination therapy in PCa to modulate CD8+ T cell responses by reducing stress response gene expression and enhancing activation markers.

MYC amplification and PTEN loss have been associated with mCRPC, with PTEN loss reported to generate a more immunosuppressive and 'cold' TME, leading to resistance to ICB therapy^{39–41}. Interestingly, comparing the scRNA-seq data from Myc-CaP WT and PTEN KO tumors, we observed that PTEN loss reduced the abundance of CD8+ T and NK cells in the TME (Supplementary Fig. 8A–C). The abundance of TAMs, especially Reg-TAMs expressing M2-like immunosuppressive markers, such as Arg1, Cd68, Mrc1, and Cd274, markedly increased in PTEN KO tumors (Supplementary Fig. 8D–F). Moreover, PTEN loss increased the expression of genes involved in mTOR signaling, protein secretion and UPR, and TNF α signaling via NF- κ B response in cancer cells (Supplementary Fig. 8G). In addition, expression of IFN response genes were downregulated in specific TAM subtypes such as IFN-Mo/M ϕ , Prolif-TAMs, Inflamm-TAMs as well as dendritic cells (Supplementary Fig. 8G). In summary, PTEN loss in Myc-CaP tumors diminishes cytotoxic immune cell populations such as CD8+ T cells and NK cells, while concurrently fostering an immunosuppressive TME, illustrating its complex role in shaping the immune landscape of PCa.

IRE1 α -XBPs pathway is negatively associated with CD8+ and NK cell infiltration in human PCa

To determine if the IRE1 α -XBPs pathway affects immune cell infiltration in the TME, we analyzed the correlation between IRE1 α or XBPs mRNA expression and CD8+ T cell infiltration in the TCGA PCa dataset. We found that PCa tumors with high IRE1 α expression had less CD8+ T cell infiltration (Supplementary Fig. 9A). Additionally, the expression of IRE1 α -XBPs target genes, such as DNAJB9 and DNAJC3, was negatively correlated with CD8+ T cell infiltration in PCa tumors (Supplementary Fig. 9B, C). Similarly, three different immune cell infiltration estimation tools suggested that tumors with high XBPs mRNA levels had significantly lower T cell infiltration (Supplementary Fig. 9D–G).

Since the abundance of NK cells were increased in the scRNA-seq data in the tumors of IRE1 α KO and MKC8866 treated animals, we also determined the potential correlation of IRE1 α -XBPs pathway with NK cell infiltration. NK cell infiltration scores were significantly higher in patients with PCa with low XBPs expression (Supplementary Fig. 9H–J). Taken together, these findings suggest that IRE1 α -XBPs pathway may play a critical role in modulating the immune microenvironment in PCa, potentially affecting NK and CD8+ T cells infiltration.

TAM gene signature is associated with unfavorable PCa prognosis

To determine the potential clinical relevance of the IRE1 α -XBPs pathway on TAMs in the TME, we assessed correlation of IRE1 α expression with macrophage markers in the TCGA PCa dataset. IRE1 α expression was positively correlated with the expression of M2

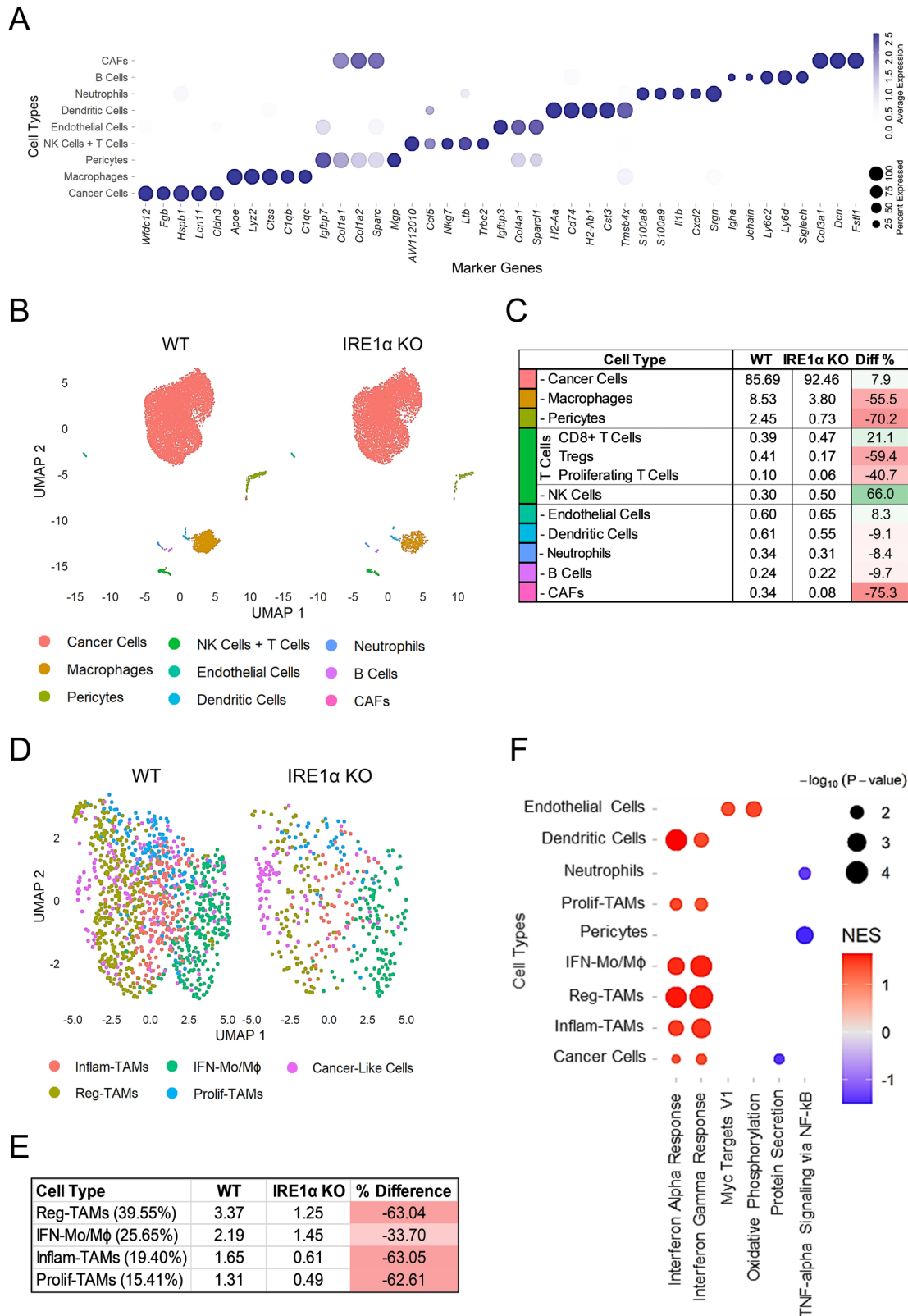
macrophage markers CD163 and MRC1 (Supplementary Fig. 10A). Validating these observations, IHC analyzes showed significantly higher CD68+ tumor infiltrating macrophages in IRE1 α high samples (Figs. 8A, B). In line with these, macrophage levels were estimated to be higher in PCa tumors with high XBPs mRNA levels (Fig. 8C)⁴².

Through the examination of 147 genes that exhibited significant downregulation in TAMs between WT and IRE1 α KO tumors (Supplementary Data 3), we identified five genes (Apoe, Clqa, Trem2, Pf4, and Mrc1) (Fig. 8D) with high expression mainly in the macrophage cluster (Supplementary Fig. 10B). These genes were combined with TAM gene markers Arg1 and Cd68, which were among the top gene markers in Reg-TAMs (Supplementary Fig. 6A), the most abundant TAM subtype within the TME that also increased in the PTEN KO Myc-CaP TME compared to wild type tumors (Supplementary Fig. 8E, F). We established a scRNA-seq derived "TAM signature" from these 7 genes. Notably, the expression of TAM signature genes was increased in the macrophage cluster in PTEN KO tumors (Supplementary Fig. 10C). Interestingly, in these tumors, combination therapy reduced the expression of TAM signature genes (Supplementary Fig. 10D), which were mainly expressed in Reg-TAMs (Supplementary Fig. 10E). Importantly, the TAM gene signature was elevated in patient samples with advanced-stage PCa, showed strong positive association with the Gleason score and negatively correlated with progression-free survival in the TCGA and disease-free survival in MSKCC PCa datasets^{15,43} (Fig. 8E–G). Collectively, these findings demonstrate a significant association of the TAM gene signature with an unfavorable outcome in PCa.

Discussion

During tumor formation, cancer cells hijack the normal stress response pathways to adapt to various stressors that impact the TME. Similar to other solid tumors, PCa cells rely on UPR signaling to survive under intra- and extra-cellular stress conditions^{16,19}. While the role of UPR in promoting cancer cell growth and malignancy is documented in various studies^{3,16,44–49}, the complex relationship between the activation of UPR in cancer cells, its influence on the TME and the anti-tumor immune responses remain largely unexplored. In this study, we have shown that inhibition of the IRE1 α signaling in PCa cells remodels the TME by increasing IFN responses and decreasing the abundance of immunosuppressive cells. Pharmacological inhibition of IRE1 α signaling also increased IFN responses and significantly improved anti-tumor immunity. These findings are significant since PCa is considered an immunologically "cold" tumor, with very limited response to immunotherapies compared with some other cancer types.

IRE1 α loss resulted in significant tumor regression and enhanced survival in mice harboring Myc-CaP tumors. scRNA-seq analysis showed that the abundance of immunosuppressive cells in the TME, such as TAMs and Tregs, were markedly reduced in IRE1 α KO tumors compared to their WT counterparts, while CD8+ T and NK cells were increased (Fig. 4; for a model, see Fig. 9). This indicates a notable



remodeling of the TME upon IRE1α loss in tumor cells. A recent study in a non-small cell lung cancer (NSCLC) mouse model found that upon IRE1α targeting, CD8+ T cells were increased and Tregs were decreased, but without significant effects on TAMs⁴⁴, suggesting that there may be both similarities and differences for the influence of tumor cell IRE1α signaling on the TME in different cancer types.

IFNs are cytokines that help the immune system eradicate pathogens and cancer cells. They activate immune cells such as NK cells, cytotoxic T cells, and macrophages, and enhance anti-tumor immunity by increasing MHC antigen presentation^{20,50-54}. Genetic or pharmacological inhibition of IRE1α led to marked increases in IFN signaling in multiple cell types in the TME, especially in antigen-

Fig. 4 | scRNA-seq analysis reveals changes in the TME landscape upon loss of IRE1 α in Pca cells. **A, B** scRNA-seq was performed from WT and IRE1 α KO (clone #2) tumors (six tumor samples per group were pooled for scRNA-seq) and cell types were clustered and annotated based on the marker genes expressed in each cell type. **A** The dot plot displays the marker genes that define each cell type that were annotated. The color intensity and size of the dots represent average gene expression and percentage expression of the specified marker genes within the respective cell type population, respectively. **B** UMAP plots show clustering of single cells from WT (11,071 cells) and IRE1 α KO (8,434 cells) single cells, with cell types represented by different colors. **C** The table shows the percentage abundance of each indicated cell type within the TME, along with the observed percentage changes between WT and IRE1 α KO tumors. **D** The UMAP plots demonstrate

subtypes of TAMs in WT and IRE1 α KO tumors. Different TAM subtypes are represented by distinct colors, based on the markers presented in Supplementary Fig. 6A. The fifth cluster, exhibiting cancer cell markers (likely resulting from doublets), was excluded from the further analysis. **E** Percentage abundance of the TAM subtypes is indicated, along with the observed percentage changes in IRE1 α KO compared to WT tumors. The percentage of each TAM sub-type in the total TAM population in WT tumors are indicated in parentheses. **F** The dot plot illustrates the results of the GSEA conducted on the indicated cell types using scRNA-seq data. It represents the normalized enrichment score (NES), with up- and down-regulated pathways color-coded in red and blue, respectively. The size of each dot corresponds to the $-\log_{10}(p\text{-value})$ of the indicated pathway for the respective cell types. For the details of statistical test used for figure (F)⁹².

presenting cells such as TAMs and DCs. It is possible that targeting IRE1 α may promote immunogenic cell death and production of IFNs in DCs to convert them into inflammatory cells, which then can stimulate T and NK cell infiltration resulting in anti-tumor immunity, similar to what has been observed for the PERK arm of UPR in melanoma cells⁵³. Further work is required to assess this possibility.

Similar to other immunologically 'cold' and immunotherapy unresponsive tumor types, Pca has a strong immunosuppressive TME, which contains scarce but high PD-1-expressing tumor infiltrating lymphocytes^{55–58}. In addition, they can have high levels of Tregs, TAMs and myeloid derived suppressor cells (MDSCs) all of which are linked to disease progression and death^{55,56,58,59}. Notably, PTEN deletion in Myc-CaP cells led to a more immunosuppressive and 'cold' TME, characterized by diminished IFN responses, lower infiltration of CD8+ T cells and NK cells, and a higher abundance of TAMs, especially M2-like macrophages with immunosuppressive marker gene expression. Remarkably, these effects were reversed by MKC8866 combined with anti-PD-1 therapy in Myc-CaP PTEN KO syngeneic mouse Pca model. Thus, our data highlight the impact of targeting IRE1 α to reprogram the TME and enhance the efficacy of anti-PD-1 immunotherapy in this advanced Pca model.

Previous reports have linked HSPA1A and HSPA1B expression in CD4+/CD8+ T cells to ICB therapy resistance in various cancers^{35,38}. Interestingly, MKC8866 + anti-PD-1 therapy reduced HSPA1A and HSPA1B expression in CD8+ T cells and increased the expression of T cell activation markers. It is important to highlight that with MKC8866 + anti-PD-1 therapy, CD8+ T cells also begin to increase the expression of various inhibitory immune checkpoint receptors such as Lag3, Pdcd1, Havcr2 (Figs. 7G, H), suggesting chronic antigen stimulation and CD8+ T cell exhaustion in the TME⁶⁰. Given ongoing clinical trials exploring dual combinations targeting LAG3, TIM-3, and PD-1/PD-L1 immune checkpoints and bispecific antibodies that simultaneously target LAG3/PD-1 or TIM-3/PD-1, combinatorial inhibition of IRE1 α and LAG3 or TIM-3, with or without PD-1/PD-L1 inhibition could significantly reprogram the TME and augment the efficacy of bispecific antibodies^{61,62}. Thus, it would be valuable to investigate whether coupling MKC8866 to anti-PD-1 or bispecific ICB antibody therapies can enhance the efficacy of ICB therapy and reverse resistance in the clinical setting, not only for Pca but also for other cancer types.

Over the past decade, the success of immunotherapies has transformed the landscape of cancer treatment for certain cancer types. However, despite sipuleucel-T being the first ever-approved cancer vaccine and the first immunotherapy licensed for Pca in 2010, it demonstrated limited success in the clinic and no other immunotherapies have been approved for Pca to date. The data we present here highlight the potential of targeting IRE1 α as a therapeutic strategy to enhance anti-PD-1 immunotherapy in Pca. Since MKC8866 is now in clinical trials (NCT03950570) in patients with advanced cancer, our results suggest that new clinical trials can be designed for Pca where immunotherapy approaches are coupled to IRE1 α targeting. Recent work has shown that targeting IRE1 α signaling increased ICB efficacy in

ovarian, breast, and colon cancer models, but not with a small molecule inhibitor in clinical trials^{63–65}; in addition, the molecular mechanisms appear to be different than we present here. Further work will be required to evaluate if MKC8866 would also synergize with ICB in other cancer types.

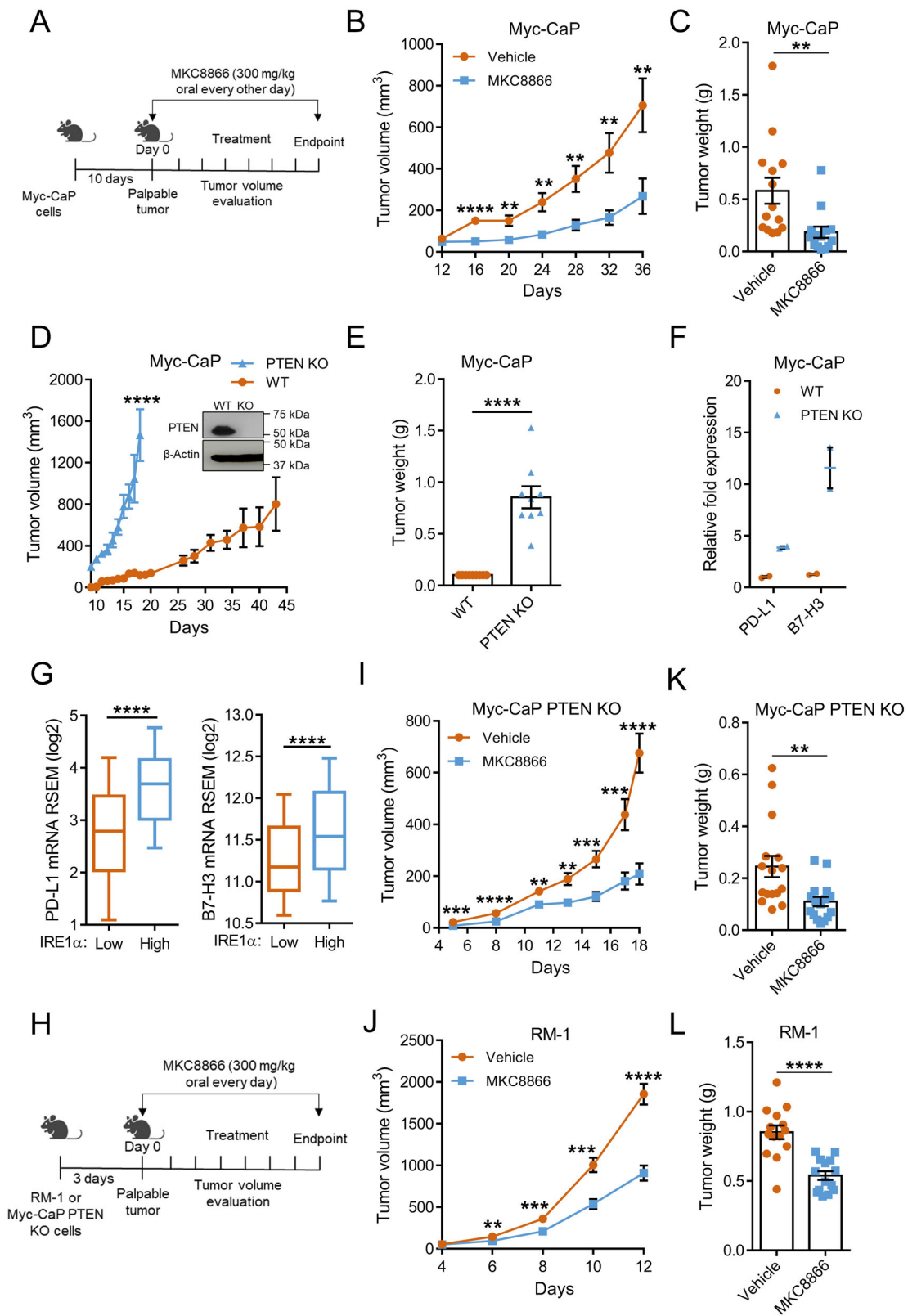
In addition to therapeutic implications, the TAM gene signature that we have identified has significant prognostic power in patients with Pca and is reduced by the MKC8866 + anti-PD-1 combination therapy; this suggests that it can potentially be useful in predicting disease course and thereby adjusting therapy options. For example, the TAM gene signature may help in stratifying patients with Pca for anti-PD-1 immunotherapy. Further work is necessary to assess these possibilities.

Previous studies have shown that IRE1 α , beyond its role in splicing XBPI, has other catalytic and non-catalytic functions. These include RIDD activity, which degrades specific target mRNAs and microRNAs, and serving as a structural determinant of mitochondria-associated membranes^{66,67}. In cancer, RIDD activity can influence tumor progression and response to therapy^{47,68}. We attempted to assess RIDD activity upon genetic or pharmacological inhibition of IRE1 α in our RNA-seq datasets. When we analyzed our data using two different RIDD activity gene signatures, developed for multiple myeloma and glioblastoma^{47,69}, the results were inconsistent, suggesting that these signatures maybe context dependent and their applicability to Pca might be limited. On the other hand, in IRE1 α KO tumors or upon MKC8866 treatment, there was significant downregulation of genes that regulate oxidative phosphorylation, which could be due to disrupted mitochondrial Ca²⁺ levels (Fig. 3F, Supplementary Figs. 4D, 7D). Further functional studies are required to investigate whether RIDD or the non-catalytic functions of IRE1 α have implications in Pca.

In summary, our findings demonstrate that activation of IRE1 α signaling in cancer cells not only has a pivotal role in cancer growth and survival, but it also reprograms the TME by modulating anti-tumor immune responses. This opens up the possibility that targeting IRE1 α may be a potential approach to improve immune therapy options for Pca, as well as for other cancer types.

Methods

Our research adheres to all applicable ethical guidelines. All animal studies were performed according to the experimental protocol (mouse strain, animal sex, age, number of animals allowed, and housing) that was approved by University of Oslo Institutional Animal Care and Use Ethical Committee (FOTS ID 27414) and the Danish Animal Experiments Inspectorate (license no. 2020-15-0201-00711). The maximal tumor size/burden was not exceeded maximum tumor size of 1 or 2 cubic centimeters for orthotopic and subcutaneous tumor models, respectively. All patient specimens were obtained with written informed consent and the approval from University of British Columbia Clinical Research Ethics Board (REB number: H21-03722) and the Norwegian Regional Committees for Medical Research Ethics South-East region (REK number S-07443a).



Cell culture

Myc-CaP (#CRL-3255) and RM-1 (#CRL-3310) cells were purchased from ATCC and cultured in DMEM supplemented with 10% fetal bovine serum (FBS), penicillin and streptomycin. Cells were maintained in a humidified incubator at 37 °C with 5% CO₂. Lack of *Mycoplasma* contamination was regularly confirmed.

CRISPR-Cas9 genome editing

To generate the IRE1 α and PTEN knock-out (KO) Myc-CaP cell lines, a guide RNA (gRNA) (5'-GCTTCATGCTGTAGCAAG-3') targeting IRE1 α or (5'-GCTAACGATCTCTTTGATGA-3') PTEN were cloned into the PX458 plasmid which expresses green fluorescent protein (GFP) as a marker⁷⁰⁻⁷². Cells were transfected in 6-well plates using Lipofectamine

Fig. 5 | MKC8866 inhibits PCa tumor growth in syngeneic PCa mouse models. **A–C** Myc-CaP cells were subcutaneously injected into FVB mice. **A** Schematic view of MKC8866 treatment. Mice were randomized and treated orally with vehicle ($n = 7$ mice, 14 tumors) or MKC8866 (300 mg/kg) ($n = 7$ mice, 14 tumors) once every two days. **B** Tumor volumes at indicated days and **(C)** tumor weights at the end of experiment. **D–F** Validation of Myc-CaP PTEN KO cell line by western analysis (inset). WT and PTEN KO cells were subcutaneously injected into FVB mice. **D** Tumor volumes are presented for WT and PTEN KO tumors ($n = 5$ mice each, 9 tumors per each group). **E** PTEN KO tumor weights were measured at day 16–18 when WT tumors were maximum 0.1 g, as indicated. **F** Myc-CaP WT and PTEN KO ($n = 2$ biological replicates per group) cells were subjected to qRT-PCR. **G** Association of PD-L1 and B7-H3 mRNA expression with IRE1 α mRNA low ($n = 160$) and high

($n = 129$) samples in the TCGA PCa dataset. **H** MKC8866 treatment strategy for Myc-CaP PTEN KO or RM-1 models. Tumor volume for **(I)** Myc-CaP PTEN KO (vehicle and MKC8866, $n = 8$ mice each, 16 tumors per group) and **(J)** RM-1 (vehicle and MKC8866, $n = 7$ mice each, 14 tumors per group) models. Same as in **(I** and **J)**, but tumor weights were measured at the end of the experiment for **(K)** Myc-CaP PTEN KO and **(L)** RM-1 models. Mean \pm standard error by two-tailed student's *t* test is presented for figure **(B, C)**, **C** ($p = 0.007$), **D** ($p = 1.06E-05$ for day 16), **E** ($p = 8.7E-07$), **I, K** ($p = 0.005$), **J**, and **L** ($p = 1.4E-05$); unpaired two-tailed Mann Whitney *t*-test is used for figure **(G)**; $**p < 0.01$, $***p < 0.001$, $****p < 0.0001$. Source data and exact *p* values are provided as a Source Data for figures **(B, I, and J)**. In box-plots, whiskers represent 10–90 percentile and middle lines indicate median of the data. Figures 5A and 5H were created in BioRender. Unal, B. (2023) BioRender.com/u75i711.

3000 (ThermoFisher Scientific). After 72 h, GFP-positive cells were FACS sorted into 96-well plates as single-cell per well. Growing cells were transferred into 24-well plates and further grown to verify their identity by assessing IRE1 α and XBP1s expression.

Lentivirus production and ectopic Xbp1s expression

HEK293T cells were transfected with pMD2.G (Addgene plasmid #12259), psPAX2 (Addgene plasmid #12260), and either pLV[Exp]-Puro-EF1A > EGFP (Vectorbuilder # VB010000-9483amc) or pLV[Exp]-EGFP-EF1A > mXbp1s (Vectorbuilder # VB900142-6935cag) using Lipofectamine 3000 (Thermo Fisher Scientific) following the manufacturer's instructions. After 12 h, the growth media was replaced. Lentiviral particles were harvested at 48 and 72 h post-transfection, filtered through a 0.2 μ m filter, and stored at -80°C . Myc-CaP IRE1 α WT and KO (clone #1) cells were infected with the lentiviral particles, and GFP-positive cells were FACS sorted into 96-well plates as single-cell per well. Individual colonies with similar levels of GFP expression were selected, and overexpression of XBP1s and its target genes expression were validated using qRT-PCR analysis.

Cell viability and colony formation assay

Myc-CaP IRE1 α wild type (WT) and knock-out (KO) clones were seeded into 96-well plates. After 72 h, cell viability was determined by the CCK-8 assay. For thapsigargin (TG) sensitivity, where indicated, cells were treated with 100 nM TG for the indicated times and cell viability was determined using the CCK-8 assay. For the colony formation assay, cells were trypsinized and seeded into 6-well plates. After 4 days, cells were fixed with methanol and stained with 0.4% crystal violet and visualized.

Apoptosis and cell cycle assay

Apoptosis assay was performed as described previously with some minor changes⁷³. Briefly, Myc-CaP IRE1 α WT and KO clones were seeded into 6 well plates. Cells were left untreated or treated with TG (100 nM) for 12 h. Alternatively, Myc-CaP cells were either treated with TG (100 nM) or MKC8866 (10 μ M) alone, or their combination for 12 h. After 12 h, cells were trypsinized and washed with cell staining buffer (Biolegend # 420201). 100 μ l of cells in Annexin V binding buffer (Biolegend # 422201) were stained with 3 μ l of 7-AAD viability staining solution (Biolegend #420404) and Annexin V (Biolegend #640953) for 15 min at room temperature. Cells were analyzed using BD LSR II Flow Cytometer. Data were analyzed using Kaluza Analysis Software (Beckman Colter Life Sciences).

Cell cycle assay was performed as described previously with some minor changes⁷⁴. Briefly, cells were resuspended by adding -20°C pre-cooled methanol drop by drop while gently vortexing. Cells were fixed overnight at -20°C in methanol. Next day, fixed cells were washed with PBS and resuspended in staining buffer (PBS containing 1.5 μ g/ml Hoechst 33258 and 100 μ g/ml RNase A). Cells were analyzed using BD LSR II Flow Cytometer. Data were analyzed using Kaluza Analysis Software (Beckman Colter Life Sciences).

Mouse studies

Briefly, 1×10^6 Myc-CaP cells were mixed 1:1 with matrigel (BD Biosciences) and the mixture was inoculated subcutaneously into 4-week-old male FVB/NRj (Janvier Labs) or nude mice (BALB/c Nu/Nu, in-house breeding) in both hind flanks. For the nude mice experiments, three animals per group was used as less variability observed in tumor growth. For MKC8866 treatment, 1×10^6 Myc-CaP cells or 0.5×10^6 Myc-CaP PTEN KO cells were injected into FVB mice as described above. For RM-1 cells, 0.5×10^6 cells were injected into 4-week-old male C57BL/6j (Janvier Labs) as described above. When the tumors were palpable, mice were randomized and either treated with vehicle (0.5% v/v hydroxypropyl-methylcellulose dissolved in water plus 0.2% v/v Tween-80, adjusted to pH 4.0) or MKC8866 (300 mg/kg) by oral gavage every other day (Myc-CaP model) or daily (Myc-CaP PTEN KO and RM-1 models) until the end of the experiment. For anti-PD-1 and MKC8866 combination treatment, 1×10^6 Myc-CaP cells were injected into FVB mice as described above. When the tumors were palpable (after 7 days of post-injection), mice were randomized and either treated with vehicle or MKC8866 (150 mg/kg) by oral gavage every other day. After 3 days of initial MKC8866 treatment, mice were treated weekly with either 10 mg/kg of anti-PD-1 (ichorbio # ICH1132UL) or anti-IgG isotype control (ichorbio # ICH2244UL) antibodies by intraperitoneal injection (IP). In PTEN KO and RM-1 models, tumor-bearing mice were treated daily with MKC8866 (300 mg/kg) along with anti-IgG or anti-PD-1 antibodies administered every three days or every two days, respectively as described above. Tumors were measured with a caliper at the indicated time points and volumes were calculated using the following formula $V = W^2 \times L \times 0.5$ (*V*, volume; *W*, width; *L*, length). Tumors were harvested at the end of the experiment and weights were determined. For survival experiments, the tumor bearing mice were euthanized when the tumor sizes reached to maximum ethically allowable limit.

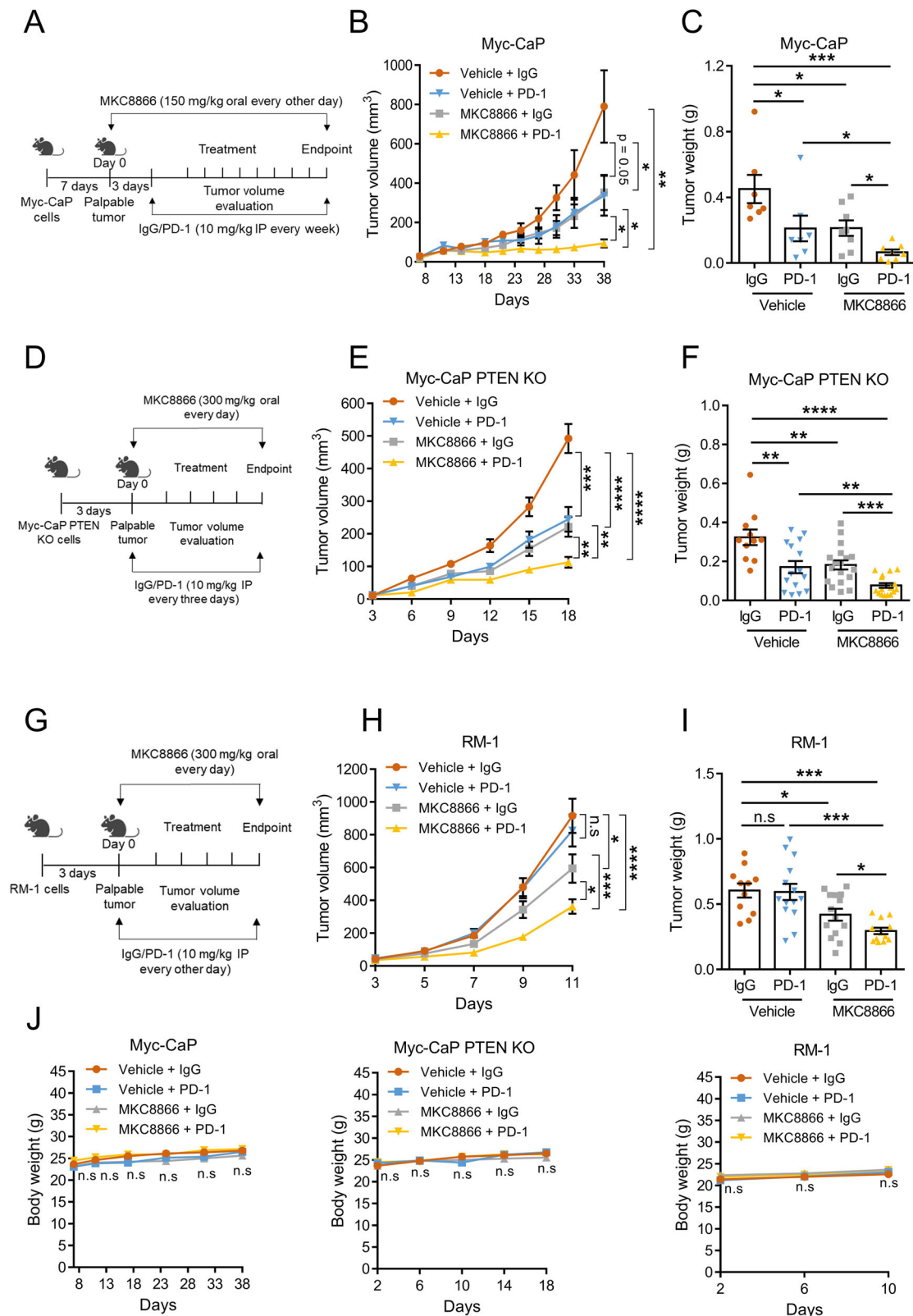
For the orthotopic Myc-CaP model, 0.5×10^6 cells were injected into the anterior prostatic lobe of FVB mice in 2/3 PBS and 1/3 Matrigel gel (Sigma #E6909). Scans were performed using a T1 weighted MRI scan before termination to evaluate the tumor volume as described previously⁷⁵.

RNA-sequencing

RNA-sequencing (RNA-seq) was performed on Myc-CaP IRE1 α WT and KO cells, as well as corresponding tumor samples from FVB mice. Briefly, RNA was isolated from the cells grown in vitro or the tumor samples using Trizol and purified using RNeasy columns (Qiagen). After RNA isolation, TruSeq stranded RNA-seq libraries were prepared according to manufacturer instructions (Illumina) and 50 bp paired-end sequencing was performed using Illumina NovaSeq (Illumina, Inc) at the NorSeq Sequencing Core (Ullevål).

RNA-seq and gene set enrichment analysis

RNA-Seq data was processed through nf-core rnaseq pipeline (version 3.6)⁷⁶. Briefly, reads were trimmed using Trimalore (version 0.6.7) and



then mapped to Grcm38 using STAR RNA-Seq aligner (version 2.6.1d). The reads were then quantified via Salmon (version 1.5.2) using Ensemble 81 as a reference transcript database. Reads were normalized via DeSeq normalization⁷⁷. Gene set enrichment analysis (GSEA) tool and Enrichr web server were used to infer pathways and gene networks of differentially expressed genes^{78–81}.

Quantitative and semi-quantitative PCR

For reverse transcription quantitative PCR (qPCR) analysis, total RNA was isolated as described above. One μ g of RNA was reverse-transcribed using Superscript II (Thermo Fisher Scientific) and diluted 1/20 in nuclease-free water. qPCR was performed as described previously⁵ from diluted cDNAs with gene specific primers

Fig. 6 | MKC8866 synergizes with anti-PD-1 immunotherapy in syngeneic PCA mouse models. A–C MKC8866 synergizes with anti-PD-1 treatment in Myc-CaP model. **A** Schematic representation of the experiment in the Myc-CaP mouse model. **B** Tumor volumes were measured at the indicated days for Vehicle + anti-IgG or Vehicle + anti-PD-1 ($n = 4$ mice, 7 tumors) and MKC8866 + anti-IgG or MKC8866 + anti-PD-1 ($n = 4$ mice, 8 tumors). **C** Same as in **(B)**, but tumor weights were measured at the end of the experiment. **D–F** MKC8866 synergizes with anti-PD-1 treatment in Myc-CaP PTEN KO model. **D** Schematic representation of the experiment. **E** Tumor volumes measured at the indicated days are shown for Vehicle + anti-IgG ($n = 6$ mice, 11 tumors), Vehicle + anti-PD-1 ($n = 8$ mice, 15 tumors), MKC8866 + anti-IgG ($n = 9$ mice, 18 tumors), and MKC8866 + anti-PD-1 ($n = 8$ mice, 16 tumors). **F** Same as in **(E)** but tumor weights at the end of the experiment are presented. **G–I** MKC8866 enhances the efficacy of anti-PD-1 treatment in the RM-1

model. **G** Schematic representation of the experiment. **H** Tumor volumes measured at the indicated days are shown for Vehicle + anti-IgG ($n = 6$ mice, 11 tumors), Vehicle + anti-PD-1 ($n = 7$ mice, 14 tumors), MKC8866 + anti-IgG ($n = 7$ mice, 14 tumors), and MKC8866 + anti-PD-1 ($n = 6$ mice, 12 tumors). **I** Same as in **(H)**, but tumor weights at the end of the experiment are presented. **J** Body weights of the mice from **(B, E, and H)** with the specified treatments for Myc-CaP, Myc-CaP PTEN KO, and RM-1 models respectively. Mean \pm standard error by two-tailed student's *t*-test is presented for figure **B, E, F, H, I, and J**; unpaired two-tailed Mann Whitney *t*-test is used for **C**; * $p < 0.05$, ** $p < 0.01$, *** $p < 0.001$, **** $p < 0.0001$, n.s., non-significant. Source data and exact *p* values are provided as a Source Data for figures **(B, C, E, F, H, I, and J)**. Figures 6A, 6D and 6G were created in BioRender. Unal, B. (2023) BioRender.com/u75i711.

(Supplementary Data 4). Relative gene expression was determined by $\Delta\Delta$ CT method by normalizing mRNA expression values to β -actin. Semi-quantitative reverse transcription PCR (RT-PCR) was performed to determine XBP1s mRNA levels. XBP1 specific primers spanning the XBP1s splicing site were used to detect both XBP1 and XBP1s transcript levels with distinct PCR products.

Western analysis

Western analysis was performed as described previously^{5,82}. Briefly, cells were lysed in RIPA buffer supplemented with protease and phosphatase inhibitor cocktail. 30 μ g of cleared protein lysate was resolved by 10% SDS-PAGE. Proteins were transferred onto a PVDF membrane (Biorad) and blocked for 1 h with 5% skim milk, followed by overnight incubation with primary antibodies from Cell Signaling, IRE1 α (#3294S; 1/1000), PTEN (#9559S; 1/1000) and β -Actin (#3700, 1/20000). Membranes were washed and incubated with secondary horseradish peroxidase-conjugated anti-rabbit IgG or anti-mouse IgG antibodies at room temperature for 1 h. ECL detection reagents (Amersham Pharmacia Biotech) were used to visualize the proteins.

IHC tissue microarray of PCA patient samples

A tissue microarray (TMA), containing benign prostate ($n = 16$) and prostate cancer ($n = 72$) samples, was obtained from Vancouver Prostate Center. TMA sections were analyzed for IRE1 α , CD68 and AR immunopositivity using Ventana Discovery Ultra autostainer (Ventana Medical Systems, Tucson, Arizona). In brief, baked and deparaffinized tissue sections were incubated in Tris-based buffer (CC1, Ventana) at 95 °C for 64 min to retrieve antigenicity, followed by incubation at room temperature with anti-IRE1 α Rabbit mAb (Clone 14C10, #3294; Cell Signaling, 1/50), CD68 Mouse mAb (Clone Kp-1, #168M-95; Cell Marque, 1/200), and AR (Clone N-20, sc-816, Santa Cruz, 1/50) for 2 h. Bound primary antibodies were visualized with the DISCOVERY Anti-Rb HQ/Anti-HQ HRP Detection Kit, DAB MAP Detection kit, and UltraMap DAB anti-Rb Detection Kit (Ventana) respectively. All stained slides were digitized with Leica scanner (Aperio AT2, Leica Microsystems; Concord, Ontario, Canada) at magnification equivalent to 40X. The images were subsequently stored in the Aperio eSlide Manager (Leica Microsystems) of the Vancouver Prostate Center. The IRE1 α and AR IHC positive areas and CD68 positive cell counts were reviewed by a research pathologist. Values on a four-point scale were assigned to IRE1 α and nuclear AR immunostaining. Descriptively, 0 represents no staining, 1 represents low, but detectable degree of staining, 2 represents clearly positive cases, and 3 represents strong expression. For IRE1 α , IHC was further quantified for staining intensity (0–3) and percentage of positive cells (0–100%). For each sample, the H-Score was calculated as staining intensity \times percentage of positive cells.

Proteomics

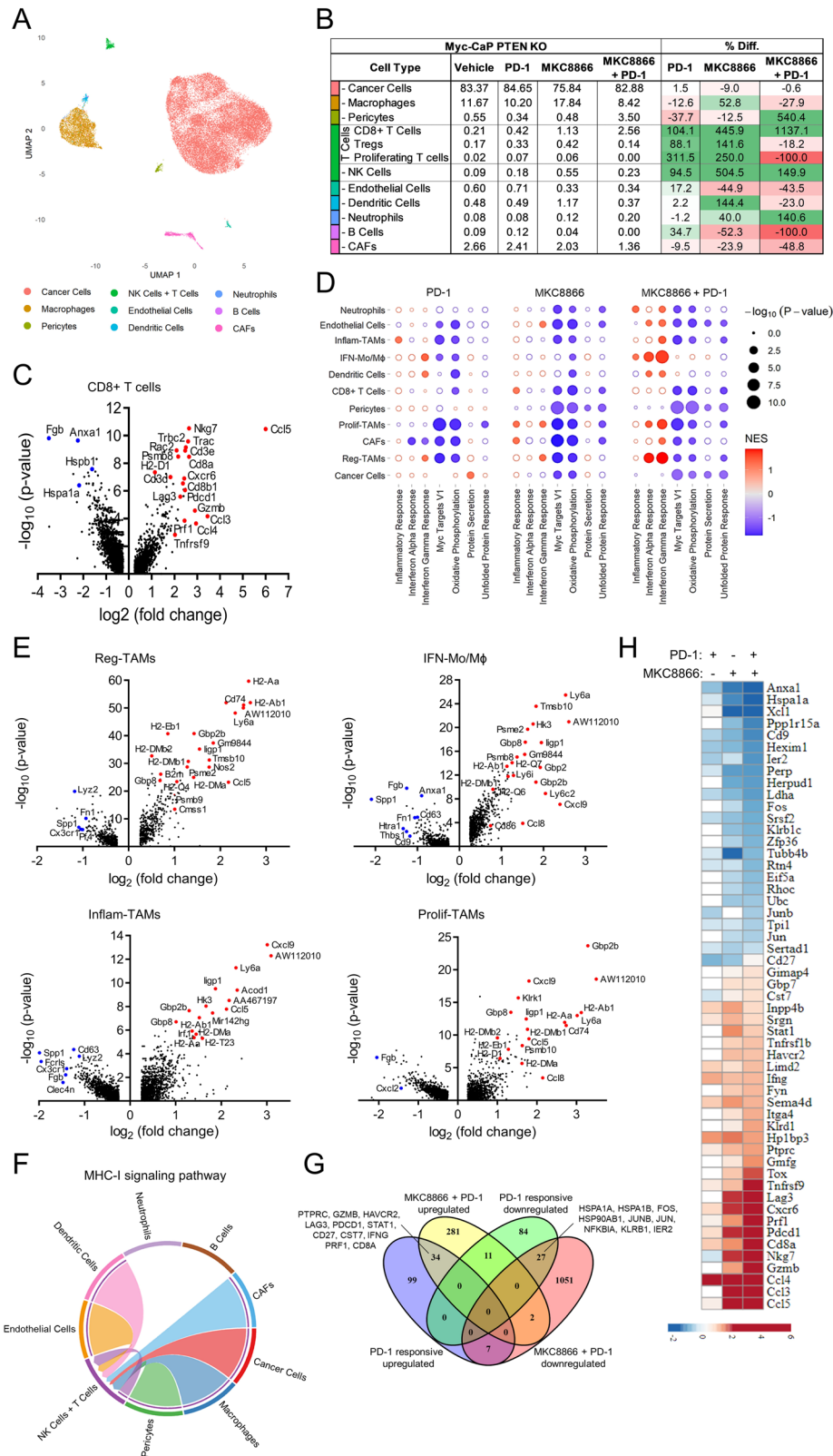
Whole tumor tissue protein extracts were prepared and subjected to an in-solution tryptic digest using a modified version of the Single-Pot

Solid-Phase-enhanced Sample Preparation (SP3) protocol^{83,84}. Eluates were added to Sera-Mag Beads (Thermo Scientific) in 10 μ l 15% formic acid and 30 μ l of ethanol and proteins were bound by shaking for 15 min at room temperature. SDS was removed by four subsequent washes with 200 μ l of 70% ethanol. Proteins were digested overnight at room temperature with 0.4 μ g of sequencing grade modified trypsin (Promega, #V5111) in 40 μ l HEPES/NaOH, pH 8.4 in the presence of 1.25 mM TCEP and 5 mM chloroacetamide (Sigma-Aldrich). Beads were separated, washed with 10 μ l of an aqueous solution of 2% DMSO and the combined eluates were dried down. Peptides were reconstituted in 10 μ l of ddH₂O and reacted for 1 h at room temperature with 40 μ g of TMTpro label reagent (Thermo Scientific) dissolved in 4 μ l of acetonitrile. Excess TMT reagent was quenched by the addition of 4 μ l of an aqueous 5% hydroxylamine solution (Sigma). Peptides were reconstituted in 0.1% formic acid, mixed to achieve a 1:1 ratio across all TMT-channels and purified by a reverse phase clean-up step (OASIS HLB 96-well μ Elution Plate, Waters #186001828BA).

Peptides were subjected to an off-line fractionation under high pH conditions yielding 12 fractions⁸³. Each fraction was analyzed by LC-MS/MS on an Orbitrap Fusion Lumos mass spectrometer (Thermo Scientific). To this end, peptides were separated using an Ultimate 3000 nano RSLC system (Dionex) equipped with a trapping cartridge (Precolumn C18 PepMap100, 5 mm, 300 μ m i.d., 5 μ m, 100 Å) and an analytical column (Acclaim PepMap 100. 75 \times 50 cm C18, 3 mm, 100 Å) connected to a nanospray-Flex ion source. The peptides were loaded onto the trap column at 30 μ l per min using solvent A (0.1% formic acid) and eluted using a gradient from 2 to 40% Solvent B (0.1% formic acid in acetonitrile) over 2 h at 0.3 μ l per min (all solvents were of LC-MS grade). The Orbitrap Fusion Lumos was operated in positive ion mode with a spray voltage of 2.4 kV and capillary temperature of 275 °C. Full scan MS spectra with a mass range of 375–1500 *m/z* were acquired in profile mode using a resolution of 120,000 (maximum fill time of 50 ms or a maximum of 4e5 ions (AGC) and a RF lens setting of 30%. Fragmentation was triggered for 3 s cycle time for peptide like features with charge states of 2–7 on the MS scan (data-dependent acquisition). Precursors were isolated using the quadrupole with a window of 0.7 *m/z* and fragmented with a normalized collision energy of 38. Fragment mass spectra were acquired in profile mode and a resolution of 30,000. Maximum fill time was set to 64 ms or an AGC target of 1e5 ions. The dynamic exclusion was set to 45 s.

Proteomics data analysis

Acquired data were analyzed using IsobarQuant⁸⁵ and Mascot V2.4 (Matrix Science) using a reverse UniProt FASTA Mus musculus database (UP000000589, downloaded in May 2016, 59,754 entries including common contaminants). The following modifications were taken into account: Carbamidomethyl (C, fixed), TMT16plex (K, fixed), Acetyl (N-term, variable), Oxidation (M, variable) and TMT16plex (N-term, variable). The mass error tolerance for full scan MS spectra was set to 10 ppm and for MS/MS spectra to 0.02 Da. A maximum of two missed cleavages were allowed. A minimum of two unique peptides



with a peptide length of at least seven amino acids and a FDR below 0.01 were required on the peptide and protein level⁸⁶.

The raw output files of IsobarQuant (protein.txt-files) were processed using the R programming language (ISBN 3-900051-07-0). Only proteins that were quantified with at least two unique peptides were considered for the analysis. 6505 proteins passed the quality control

filters. Raw TMT reporter ion intensities ('signal_sum' columns) were first cleaned for batch effects using limma⁸⁷ and further normalized using vsn (variance stabilization normalization)⁸⁸. Proteins were tested for differential expression using the limma package. The replicate information was added as a factor in the design matrix given as an argument to the 'lmFit' function of limma. A protein was annotated as a

Fig. 7 | MKC8866 + anti-PD-1 combination therapy reprograms the TME landscape and enhances CD8+ T and NK cell infiltration. scRNA-seq was performed on tumor samples from the experiment presented in Fig. 6D and E (six tumor samples per group were pooled for scRNA-seq). **A** Different colors in the UMAP plot represent the assigned cell types identified based on the marker genes in Supplementary Fig. 7 A. **B** The table displays the percentage abundance of each cell type within the TME and the observed percentage changes for the different treatments compared to vehicle. **C** Volcano plot indicates the up- and down-regulated genes in the CD8+ T cell cluster in the scRNA-seq data from tumor samples of mice treated with MKC8866 + anti-PD-1 compared with vehicle. Notable up- and down-regulated genes were highlighted as red and blue, respectively. **D** The dot plot displays selected GSEA results (for hallmark gene sets) from scRNA-seq data for the different treatments compared to vehicle. Significantly up- or down-regulated pathways are depicted in red and blue, respectively. Dot size corresponds to the $-\log_{10}$ (p -value) of each pathway for the respective cell type. **E** Volcano plots indicate the up- and

down-regulated genes in the indicated TAM subtypes for combination therapy vs vehicle. Notable up- and down-regulated genes are highlighted as red and blue, respectively. **F** Chord plot displaying the result from CellChat analyzes showing the MHC-I signaling pathway interaction between indicated cell types from tumor samples of mice treated with combination therapy. **G** The Venn diagram summarizes the differentially expressed genes ($p < 0.05$) that were significantly altered in the CD8+ T cell cluster from tumors of combination therapy compared to the differentially expressed genes ($p < 0.05$) in the scRNA-seq data from the CD8+ T cell cluster in pembrolizumab + enzalutamide responsive versus non-responsive mCRPC patient samples as reported previously³⁵. **H** The heatmap indicates the \log_2 fold-change expression of overlapping genes from Figure G in the CD8+ T cell cluster from tumors of mice for the indicated treatments compared to vehicle treatment. The Wilcoxon rank-sum test implemented in Seurat was used for Figures (C, E, and G).

hit with a false discovery rate (fdr) $< 5\%$ and a fold-change of at least 100% and as a candidate with a fdr below 20% and a fold-change of at least 50%.

Single-cell suspension of tumor samples for scRNA-seq

Freshly dissected tumor samples were washed with PBS and transferred into GEXSCOPE Tissue Preservation Solution (Singleron), and stored on ice. 6 tumor samples from each group were pooled for scRNA-seq. The tissue samples were then washed with Hanks balanced salt solution three times and minced into small pieces which were digested with Tissue Dissociation Solution (Singleron) at 37 °C for 15 min with agitation. After digestion, cells were passed through a 40 μm strainer to remove cell debris and centrifuged at 300 $\times g$ for 5 min. The supernatant was removed and cell pellet was resuspended in 1 ml PBS, followed by red blood cell lysis using RBC lysis buffer. Next, cells were centrifuged at 500 $\times g$ for 5 min and resuspended in PBS. The viability and cell count were determined by trypan blue staining under microscope. Cell viability exceeded 80% for each sample.

scRNA-seq library preparation

The single-cell suspension was adjusted to a concentration of 1×10^5 / ml for library preparation. This was loaded onto microfluidics chips (GEXSCOPE Single-Cell RNA-seq Kit, Singleron Biotechnologies) and GEXSCOPE 3' SD scRNA-seq libraries were prepared according to manufacturer instructions (Singleron Biotechnologies). Individual libraries were diluted and pooled for next generation sequencing on Illumina NovaSeq with 150 bp paired-end reads.

scRNA-seq data analysis

The sequencing reads were aligned to mouse reference Grcm38 genome and Singleron Telescope tool (<https://github.com/singleron-RD/CeleScope>) were used to generate the gene expression matrices. Gene expression levels were analyzed by counting the unique molecular indices (UMIs) detected in each cell. We applied quality control measures to the data. Only cells with a library size of at least 1,000 counts and falling within the 95 percent confidence interval for the prediction of mitochondrial content ratio and detected genes in proportion to the cell's library size were retained. In addition, cells with mitochondrial proportions greater than 10% were removed. To normalize, scale, and reduce the dimensionality of the scRNA-seq data, Seurat was used with default functions and parameters, including Principal Component Analysis (PCA)⁸⁹. Harmony was used for data integration, and the top 50 dimensions returned by Harmony were used to generate UMAP projections of the data⁹⁰. Cell clustering was performed using Seurat's built-in functions, with default

resolution and utilizing the Harmony embedding as the basis for constructing the nearest neighbor network. Cell identities were assigned through differential expression analysis and manual inspection of cell type-specific marker genes. For visualizing quantitative gene expression and specific gene expression patterns, R packages ggplot2 and Nebulosa were employed⁹¹. GSEA analysis was performed as described previously⁹².

Cell-cell communication across different experimental conditions was analyzed using the CellChat R package. Initially, a Seurat object containing all treatment data was integrated to serve as input for generating a CellChat object, utilizing the count data and associated metadata. For reference, the CellChatDB.mouse database was employed to identify known signaling pathways and interactions relevant to mouse cell communication. The dataset was subsetted to align with the reference, enabling the detection of overexpressed genes and interactions potentially involved in cell communication. Communication probabilities were calculated at both the interaction and pathway levels, and interactions involving fewer than ten cells were excluded to ensure robust results. An aggregated network of interactions was then constructed and analyzed to compute centrality measures, which identified the key roles of specific cell types or interactions within the network. This methodology was applied to multiple subsets of the Seurat object, each representing distinct experimental conditions. For each experimental group, bubble plots and heatmaps were generated to highlight significant interactions. A predefined list of signaling pathway for "MHC-I" was examined for each experimental conditions. Chord diagrams were created to visualize interactions, providing a clear depiction of cell-cell communication dynamics under each experimental scenario.

Bioinformatics analysis

Raw data for PCa RNA-seq were downloaded from the TCGA website. Raw reads were processed through the nf-core rnaseq pipeline (version 3.6)⁷⁶. Briefly, reads were trimmed using Trimalore (version 0.6.7), and then mapped to Grch38 using the STAR RNA-Seq aligner (version 2.6.1d). Finally, XBPIs reads were obtained from the STAR's splice junction output file (SJ.out.tab files) using the following coordinates: Chr22:28796128-28796153. XBPIs specific reads were normalized to the total number of mapped read counts. Next, using normalized spliced XBPIs reads, samples were divided into low ($n = 200$) and high ($n = 200$) expressing groups. GSEA was performed as previously described⁷⁸. Immune cell infiltration analysis was performed by downloading the TCGA PCa infiltration estimation data from the TIMER2.0 website⁹³. Immune cell infiltration estimation scores of XBPIs low and high expressing PCa were extracted and analyzed.

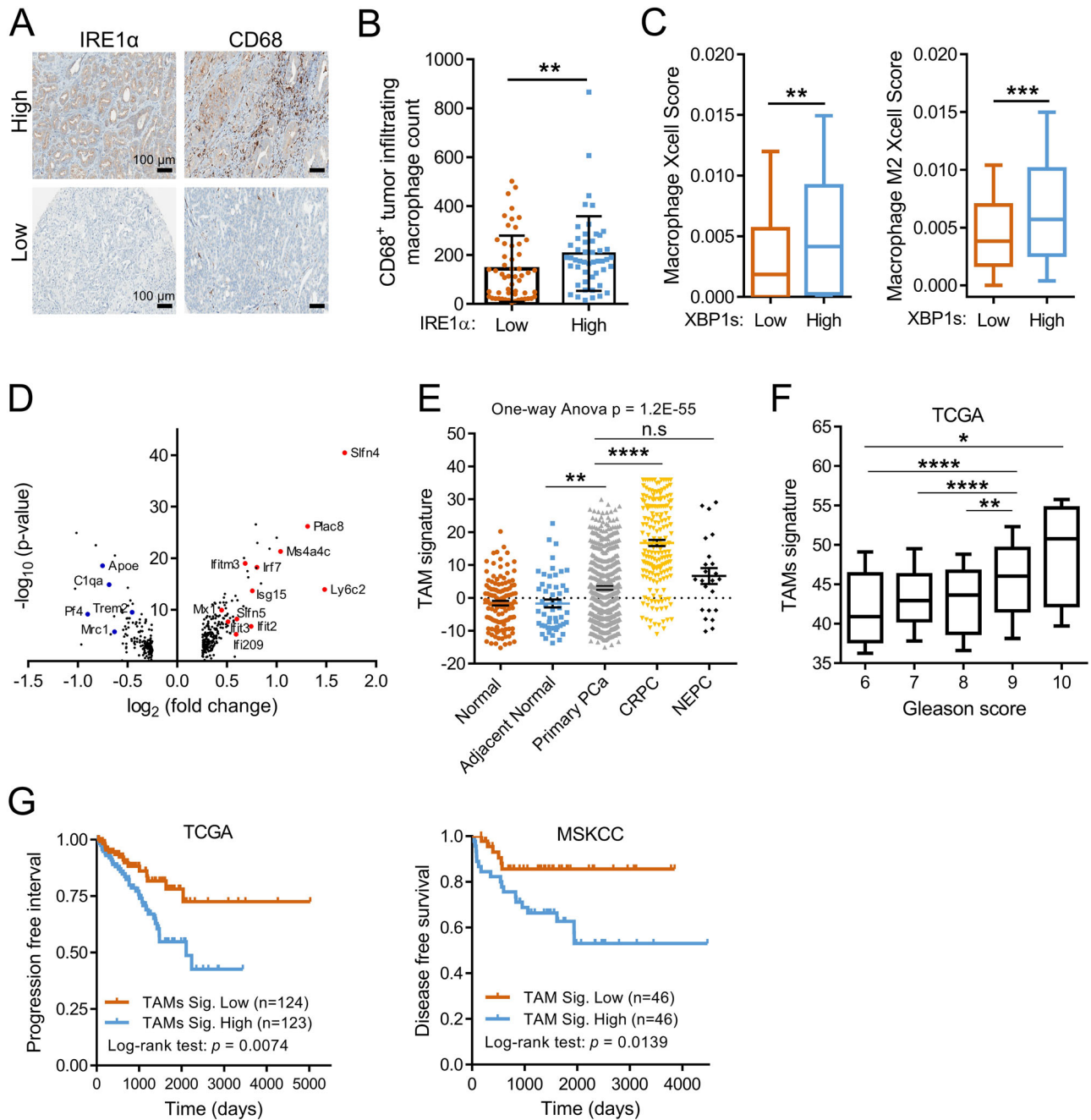


Fig. 8 | A TAM gene signature derived from scRNA-seq data is strongly associated with poor prognosis in patients with PCA. A Representative images are shown for IRE1α and CD68 IHC staining in human PCA specimens. **B** Quantification of CD68⁺ tumor infiltrating macrophages [IRE1α low ($n = 54$) and high ($n = 49$)] is presented for human PCA tumor samples. **C** Xcell macrophage and M2 macrophage infiltration scores of TCGA PCA tumors divided according to XBP1s low ($n = 200$) and high ($n = 200$) expression similar to in Fig. 1F. **D** Volcano plot indicates the up- and down-regulated genes in the main macrophage (TAMs) cluster in the scRNA-seq data that was shown in Fig. 4B–E. **E** TAM gene signature expression in the indicated PCA patients from the publicly available datasets¹⁴. Normal prostate tissue (GTEx): $n = 119$; Tumor adjacent normal (TCGA): $n = 52$; Primary PCa (TCGA): $n = 499$; CRPC: $n = 183$; NEPC: $n = 23$. **F** PCA patients with high Gleason score [Gleason 6

($n = 45$), 7 ($n = 247$), 8 ($n = 64$), 9 ($n = 137$), and 10 ($n = 4$)] exhibit an elevated TAM gene signature score in the TCGA PCA dataset. **G** Kaplan-Meier plots illustrate a positive correlation between increased expression of the TAM signature (depicted as blue) and significantly shorter progression free survival in the TCGA dataset, and shorter disease-free survival in MSKCC PCA datasets. Mean \pm standard error by unpaired two-tailed Mann-Whitney t -test is presented for **B** ($p = 0.006$), **(C)** ($p = 0.002$ for left and $p = 0.0003$ for right figures), and **(E)** (Adjacent Normal vs Primary PCa: $p = 0.002$); one-way Anova is used for figure **(F)** (source data and exact p values are provided as a Source Data); * $p < 0.05$, ** $p < 0.01$, *** $p < 0.001$, **** $p < 0.0001$. In box-plots, whiskers represent 10–90 percentile and middle lines indicate median of the data. The Wilcoxon rank-sum test implemented in Seurat was used for **D**.

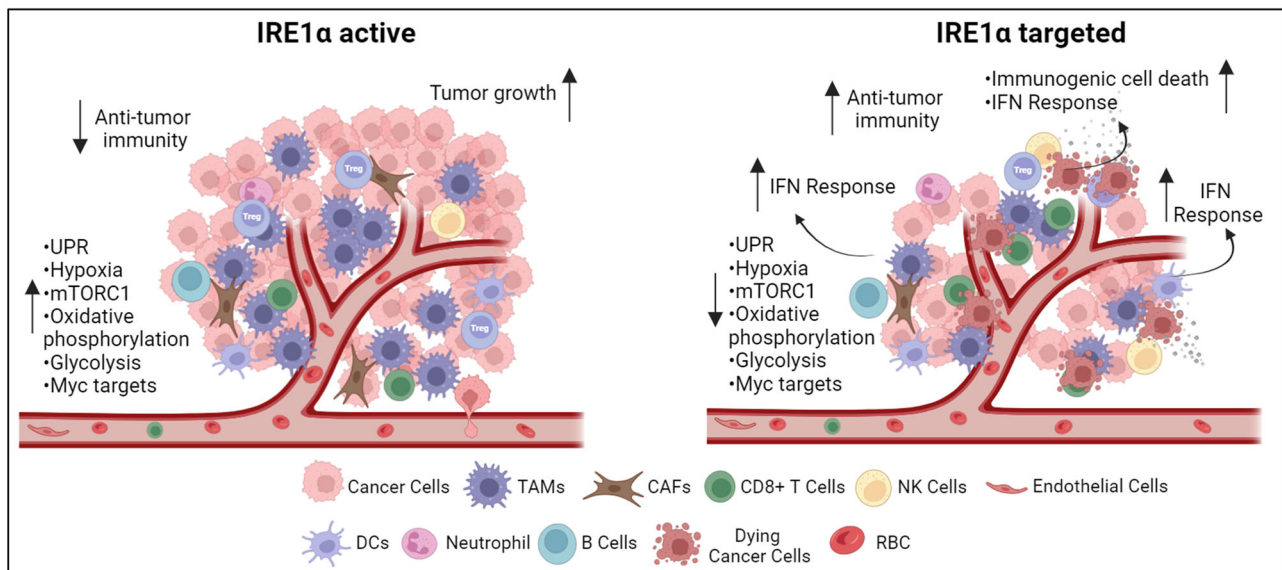


Fig. 9 | Schematic summary of the main findings of the study. IRE1 α activation in cancer cells inhibits the IFN responses and fosters the accumulation of immunosuppressive cells such as TAMs and Tregs within the TME. This hinders the ability to mount an effective anti-tumor immune response that results in tumor progression. IRE1 α genetic targeting in cancer cells or combination therapy (MKC8866 + anti-

PD-1) augments the IFN responses in antigen-presenting cells, such as TAMs and DCs, and also decreases the abundance of immunosuppressive cells within the TME. This facilitates robust anti-tumor immune responses, effectively impeding tumor growth. Created in BioRender. Unal, B. (2023) BioRender.com/u75i71l.

Reporting summary

Further information on research design is available in the Nature Portfolio Reporting Summary linked to this article.

Data availability

RNA-seq and scRNA-seq data generated in this study have been deposited in the GEO database with the accession code [GSE240383](https://www.ncbi.nlm.nih.gov/geo/query/acc.cgi?acc=GSE240383). Publicly available RNA-seq datasets were used with accession code [GSE141633](https://www.ncbi.nlm.nih.gov/geo/query/acc.cgi?acc=GSE141633) and TCGA primary PCa raw data was downloaded from Genomic Data Commons Data Portal [<https://portal.gdc.cancer.gov/>]. The mass spectrometry proteomics data generated in this study have been deposited to the ProteomeXchange Consortium via the PRIDE partner repository with the dataset identifier [PXD044287](https://proteomecentral.proteomex.org/submitter/PXD044287). Immune cell infiltration estimation data for PCa patient samples was downloaded from TIMER2.0 website [<http://timer.cistrome.org/>]. The remaining data are available within the Article, Supplementary Information or Source Data file. Source data are provided with this paper.

References

- Walter, P. & Ron, D. The unfolded protein response: from stress pathway to homeostatic regulation. *Science* **334**, 1081–1086 (2011).
- Hetz, C., Zhang, K. & Kaufman, R. J. Mechanisms, regulation and functions of the unfolded protein response. *Nat. Rev. Mol. Cell Biol.* **21**, 421–438 (2020).
- Marciniak, S. J., Chambers, J. E. & Ron, D. Pharmacological targeting of endoplasmic reticulum stress in disease. *Nat. Rev. Drug Discov.* **21**, 115–140 (2022).
- Sheng, X. et al. Divergent androgen regulation of unfolded protein response pathways drives prostate cancer. *EMBO Mol. Med.* **7**, 788–801 (2015).
- Sheng, X. et al. IRE1 α -XBP1s pathway promotes prostate cancer by activating c-MYC signaling. *Nat. Commun.* **10**, 323 (2019).
- Di Conza, G., Ho, P. C., Cubillos-Ruiz, J. R. & Huang, S. C. Control of immune cell function by the unfolded protein response. *Nat. Rev. Immunol.* **23**, 546–562 (2023).
- Martinon, F., Chen, X., Lee, A. H. & Glimcher, L. H. TLR activation of the transcription factor XBP1 regulates innate immune responses in macrophages. *Nat. Immunol.* **11**, 411–418 (2010).
- Mogilenko, D. A. et al. Metabolic and innate immune cues merge into a specific inflammatory response via the UPR. *Cell* **178**, 263 (2019).
- Chopra, S. et al. IRE1 α -XBP1 signaling in leukocytes controls prostaglandin biosynthesis and pain. *Science* **365**. <https://doi.org/10.1126/science.aau6499> (2019).
- Chen, X. & Cubillos-Ruiz, J. R. Endoplasmic reticulum stress signals in the tumour and its microenvironment. *Nat. Rev. Cancer* **21**, 71–88 (2021).
- Dong, H. et al. The IRE1 endoplasmic reticulum stress sensor activates natural killer cell immunity in part by regulating c-Myc. *Nat. Immunol.* **20**, 865–878 (2019).
- Cubillos-Ruiz, J. R. et al. ER stress sensor XBP1 controls anti-tumor immunity by disrupting dendritic cell homeostasis. *Cell* **161**, 1527–1538 (2015).
- Song, M. et al. IRE1 α -XBP1 controls T cell function in ovarian cancer by regulating mitochondrial activity. *Nature* **562**, 423–428 (2018).
- Phillips, J. W. et al. Pathway-guided analysis identifies Myc-dependent alternative pre-mRNA splicing in aggressive prostate cancers. *Proc. Natl Acad. Sci. USA* **117**, 5269–5279 (2020).
- Cancer Genome Atlas Research, N. The molecular taxonomy of primary prostate cancer. *Cell* **163**, 1011–1025 (2015).
- Jin, Y. & Saatcioglu, F. Targeting the unfolded protein response in hormone-regulated cancers. *Trends Cancer* **6**, 160–171 (2020).
- Watson, P. A. et al. Context-dependent hormone-refractory progression revealed through characterization of a novel murine prostate cancer cell line. *Cancer Res* **65**, 11565–11571 (2005).
- Ellwood-Yen, K. et al. Myc-driven murine prostate cancer shares molecular features with human prostate tumors. *Cancer Cell* **4**, 223–238 (2003).

19. de la Calle, C. M., Shee, K., Yang, H., Lonergan, P. E. & Nguyen, H. G. The endoplasmic reticulum stress response in prostate cancer. *Nat. Rev. Urol.* **19**, 708–726 (2022).
20. Gocher, A. M., Workman, C. J. & Vignali, D. A. A. Interferon-gamma: teammate or opponent in the tumour microenvironment? *Nat. Rev. Immunol.* **22**, 158–172 (2022).
21. Ayers, M. et al. IFN-gamma-related mRNA profile predicts clinical response to PD-1 blockade. *J. Clin. Invest* **127**, 2930–2940 (2017).
22. Ma, R. Y., Black, A. & Qian, B. Z. Macrophage diversity in cancer revisited in the era of single-cell omics. *Trends Immunol.* **43**, 546–563 (2022).
23. Robinson, D. et al. Integrative clinical genomics of advanced prostate cancer. *Cell* **161**, 1215–1228 (2015).
24. Grasso, C. S. et al. The mutational landscape of lethal castration-resistant prostate cancer. *Nature* **487**, 239–243 (2012).
25. Abida, W. et al. Genomic correlates of clinical outcome in advanced prostate cancer. *Proc. Natl Acad. Sci. USA* **116**, 11428–11436 (2019).
26. Anker, J. F. et al. Multi-faceted immunomodulatory and tissue-tropic clinical bacterial isolate potentiates prostate cancer immunotherapy. *Nat. Commun.* **9**, 1591 (2018).
27. Shi, W. et al. Immune checkpoint B7-H3 is a therapeutic vulnerability in prostate cancer harboring PTEN and TP53 deficiencies. *Sci. Transl. Med* **15**, eadf6724 (2023).
28. Baley, P. A., Yoshida, K., Qian, W., Sehgal, I. & Thompson, T. C. Progression to androgen insensitivity in a novel in vitro mouse model for prostate cancer. *J. Steroid Biochem Mol. Biol.* **52**, 403–413 (1995).
29. Ribas, A. & Wolchok, J. D. Cancer immunotherapy using checkpoint blockade. *Science* **359**, 1350–1355 (2018).
30. de Almeida, D. V. P., Fong, L., Rettig, M. B. & Autio, K. A. Immune checkpoint blockade for prostate cancer: niche role or next breakthrough? *Am. Soc. Clin. Oncol. Educ. Book* **40**, 1–18 (2020).
31. Sharma, P. et al. Nivolumab plus ipilimumab for metastatic castration-resistant prostate cancer: preliminary analysis of patients in the checkmate 650 trial. *Cancer Cell* **38**, 489–499.e483 (2020).
32. PD-1 Blockade falls short (Repeatedly) in prostate cancer. *Cancer Discov.* **13**, 1032–1033. <https://doi.org/10.1158/2159-8290.CD-NB2023-0017> (2023).
33. Powles, T. et al. Atezolizumab with enzalutamide versus enzalutamide alone in metastatic castration-resistant prostate cancer: a randomized phase 3 trial. *Nat. Med* **28**, 144–153 (2022).
34. Graf, R. P. et al. Comparative effectiveness of immune checkpoint inhibitors vs chemotherapy by tumor mutational burden in metastatic castration-resistant prostate cancer. *JAMA Netw. Open* **5**, e225394 (2022).
35. Guan, X. et al. Androgen receptor activity in T cells limits checkpoint blockade efficacy. *Nature* **606**, 791–796 (2022).
36. Song, A., Nikolcheva, T. & Krensky, A. M. Transcriptional regulation of RANTES expression in T lymphocytes. *Immunol. Rev.* **177**, 236–245 (2000).
37. Sica, A. & Mantovani, A. Macrophage plasticity and polarization: in vivo veritas. *J. Clin. Invest* **122**, 787–795 (2012).
38. Chu, Y. et al. Pan-cancer T cell atlas links a cellular stress response state to immunotherapy resistance. *Nat. Med* **29**, 1550–1562 (2023).
39. Peng, W. et al. Loss of PTEN promotes resistance to T cell-mediated immunotherapy. *Cancer Discov.* **6**, 202–216 (2016).
40. Bezzi, M. et al. Diverse genetic-driven immune landscapes dictate tumor progression through distinct mechanisms. *Nat. Med* **24**, 165–175 (2018).
41. Qi, Z. et al. Overcoming resistance to immune checkpoint therapy in PTEN-null prostate cancer by intermittent anti-PI3Kalpha/beta/delta treatment. *Nat. Commun.* **13**, 182 (2022).
42. Aran, D., Hu, Z. & Butte, A. J. xCell: digitally portraying the tissue cellular heterogeneity landscape. *Genome Biol.* **18**, 220 (2017).
43. Taylor, B. S. et al. Integrative genomic profiling of human prostate cancer. *Cancer Cell* **18**, 11–22 (2010).
44. Crowley, M. J. P. et al. Tumor-intrinsic IRE1alpha signaling controls protective immunity in lung cancer. *Nat. Commun.* **14**, 120 (2023).
45. Mandula, J. K. et al. Ablation of the endoplasmic reticulum stress kinase PERK induces paraptosis and type I interferon to promote anti-tumor T cell responses. *Cancer Cell* **40**, 1145–1160.e1149 (2022).
46. Raymundo, D. P. et al. Pharmacological targeting of IRE1 in cancer. *Trends Cancer* **6**, 1018–1030 (2020).
47. Lhomond, S. et al. Dual IRE1 RNase functions dictate glioblastoma development. *EMBO Mol. Med.* **10**. <https://doi.org/10.15252/emmm.201707929> (2018).
48. Logue, S. E. et al. Inhibition of IRE1 RNase activity modulates the tumor cell secretome and enhances response to chemotherapy. *Nat. Commun.* **9**, 3267 (2018).
49. Zhao, N. et al. Pharmacological targeting of MYC-regulated IRE1/XBP1 pathway suppresses MYC-driven breast cancer. *J. Clin. Invest* **128**, 1283–1299 (2018).
50. Pestka, S., Krause, C. D. & Walter, M. R. Interferons, interferon-like cytokines, and their receptors. *Immunol. Rev.* **202**, 8–32 (2004).
51. Zitvogel, L., Galluzzi, L., Kepp, O., Smyth, M. J. & Kroemer, G. Type I interferons in anticancer immunity. *Nat. Rev. Immunol.* **15**, 405–414 (2015).
52. Fenton, S. E., Saleiro, D. & Plataniias, L. C. Type I and II interferons in the anti-tumor immune response. *Cancers (Basel)* **13**. <https://doi.org/10.3390/cancers13051037> (2021).
53. Diamond, M. S. et al. Type I interferon is selectively required by dendritic cells for immune rejection of tumors. *J. Exp. Med* **208**, 1989–2003 (2011).
54. Fuertes, M. B. et al. Host type I IFN signals are required for antitumor CD8+ T cell responses through CD8alpha+ dendritic cells. *J. Exp. Med* **208**, 2005–2016 (2011).
55. Strasner, A. & Karin, M. Immune infiltration and prostate cancer. *Front Oncol.* **5**, 128 (2015).
56. Ebel, K. et al. Prostate cancer lesions are surrounded by FOXP3+, PD-1+ and B7-H1+ lymphocyte clusters. *Eur. J. Cancer* **45**, 1664–1672 (2009).
57. Sfanos, K. S. et al. Human prostate-infiltrating CD8+ T lymphocytes are oligoclonal and PD-1+. *Prostate* **69**, 1694–1703 (2009).
58. Valdman, A. et al. Distribution of Foxp3-, CD4- and CD8-positive lymphocytic cells in benign and malignant prostate tissue. *APMIS* **118**, 360–365 (2010).
59. Hirz, T. et al. Dissecting the immune suppressive human prostate tumor microenvironment via integrated single-cell and spatial transcriptomic analyses. *Nat. Commun.* **14**, 663 (2023).
60. Blank, C. U. et al. Defining T cell exhaustion. *Nat. Rev. Immunol.* **19**, 665–674 (2019).
61. Luke, J. J. et al. The PD-1- and LAG-3-targeting bispecific molecule tebotelimab in solid tumors and hematologic cancers: a phase 1 trial. *Nat. Med* **29**, 2814–2824 (2023).
62. Clancy-Thompson, E. et al. 461Generation of AZD7789, a novel PD-1 and TIM-3 targeting bispecific antibody, which binds to a differentiated epitope of TIM-3. *J. Immunother. Cancer* **10**, A481–A481 (2022).
63. Liu, L. et al. Ablation of ERO1A induces lethal endoplasmic reticulum stress responses and immunogenic cell death to activate anti-tumor immunity. *Cell Rep. Med* **4**, 101206 (2023).
64. Guttman, O. et al. Antigen-derived peptides engage the ER stress sensor IRE1alpha to curb dendritic cell cross-presentation. *J. Cell Biol.* **221**. <https://doi.org/10.1083/jcb.202111068> (2022).
65. Lin, J. et al. Targeting the IRE1alpha/XBP1s pathway suppresses CARM1-expressing ovarian cancer. *Nat. Commun.* **12**, 5321 (2021).

66. Carreras-Sureda, A. et al. Non-canonical function of IRE1 α determines mitochondria-associated endoplasmic reticulum composition to control calcium transfer and bioenergetics. *Nat. Cell Biol.* **21**, 755–767 (2019).
67. Le Goupil, S., Laprade, H., Aubry, M. & Chevet, E. Exploring the IRE1 interactome: from canonical signaling functions to unexpected roles. *J. Biol. Chem.* **300**, 107169 (2024).
68. Maurel, M., Chevet, E., Tavernier, J. & Gerlo, S. Getting RIDD of RNA: IRE1 in cell fate regulation. *Trends Biochem Sci.* **39**, 245–254 (2014).
69. Quwaider, D. et al. RNA sequencing identifies novel regulated IRE1-dependent decay targets that affect multiple myeloma survival and proliferation. *Exp. Hematol. Oncol.* **11**, 18 (2022).
70. Hinte, F., van Anken, E., Tirosh, B. & Brune, W. Repression of viral gene expression and replication by the unfolded protein response effector XBP1u. *Elife* **9**. <https://doi.org/10.7554/eLife.51804> (2020)
71. Ran, F. A. et al. Genome engineering using the CRISPR-Cas9 system. *Nat. Protoc.* **8**, 2281–2308 (2013).
72. Xue, W. et al. CRISPR-mediated direct mutation of cancer genes in the mouse liver. *Nature* **514**, 380–384 (2014).
73. Crowley, L. C., Marfell, B. J., Scott, A. P. & Waterhouse, N. J. Quantitation of Apoptosis and Necrosis by Annexin V Binding, Propidium Iodide Uptake, and Flow Cytometry. *Cold Spring Harb. Protoc.* **2016**. <https://doi.org/10.1101/pdb.prot087288> (2016)
74. Jin, Y. et al. STAMP2 increases oxidative stress and is critical for prostate cancer. *EMBO Mol. Med.* **7**, 315–331 (2015).
75. Cai, H. et al. CRISPR/Cas9 model of prostate cancer identifies Kmt2c deficiency as a metastatic driver by Odam/Cabs1 gene cluster expression. *Nat. Commun.* **15**, 2088 (2024).
76. Ewels, P. A. et al. The nf-core framework for community-curated bioinformatics pipelines. *Nat. Biotechnol.* **38**, 276–278 (2020).
77. Love, M. I., Huber, W. & Anders, S. Moderated estimation of fold change and dispersion for RNA-seq data with DESeq2. *Genome Biol.* **15**, 550 (2014).
78. Subramanian, A. et al. Gene set enrichment analysis: a knowledge-based approach for interpreting genome-wide expression profiles. *Proc. Natl Acad. Sci. USA* **102**, 15545–15550 (2005).
79. Chen, E. Y. et al. Enrichr: interactive and collaborative HTML5 gene list enrichment analysis tool. *BMC Bioinforma.* **14**, 128 (2013).
80. Kuleshov, M. V. et al. Enrichr: a comprehensive gene set enrichment analysis web server 2016 update. *Nucleic Acids Res* **44**, W90–W97 (2016).
81. Xie, Z. et al. Gene set knowledge discovery with enrichr. *Curr. Protoc.* **1**, e90 (2021).
82. Sikkeland, J. et al. STAMP2 suppresses autophagy in prostate cancer cells by modulating the integrated stress response pathway. *Am. J. Cancer Res* **12**, 327–336 (2022).
83. Hughes, C. S. et al. Ultrasensitive proteome analysis using paramagnetic bead technology. *Mol. Syst. Biol.* **10**, 757 (2014).
84. Moggridge, S., Sorensen, P. H., Morin, G. B. & Hughes, C. S. Extending the compatibility of the SP3 paramagnetic bead processing approach for proteomics. *J. Proteome Res* **17**, 1730–1740 (2018).
85. Franken, H. et al. Thermal proteome profiling for unbiased identification of direct and indirect drug targets using multiplexed quantitative mass spectrometry. *Nat. Protoc.* **10**, 1567–1593 (2015).
86. Savitski, M. M., Wilhelm, M., Hahne, H., Kuster, B. & Bantscheff, M. A scalable approach for protein false discovery rate estimation in large proteomic data sets. *Mol. Cell Proteom.* **14**, 2394–2404 (2015).
87. Ritchie, M. E. et al. limma powers differential expression analyses for RNA-sequencing and microarray studies. *Nucleic Acids Res* **43**, e47 (2015).
88. Huber, W., von Heydebreck, A., Sultmann, H., Poustka, A. & Vingron, M. Variance stabilization applied to microarray data calibration and to the quantification of differential expression. *Bioinformatics* **18**, S96–S104 (2002).
89. Butler, A., Hoffman, P., Smibert, P., Papalexi, E. & Satija, R. Integrating single-cell transcriptomic data across different conditions, technologies, and species. *Nat. Biotechnol.* **36**, 411–420 (2018).
90. Korsunsky, I. et al. Fast, sensitive and accurate integration of single-cell data with harmony. *Nat. Methods* **16**, 1289–1296 (2019).
91. Alquicira-Hernandez, J. & Powell, J. E. Nebulosa recovers single-cell gene expression signals by kernel density estimation. *Bioinformatics* **37**, 2485–2487 (2021).
92. Gennady Korotkevich, V. S., Nikolay Budin, Boris Shpak, Maxim N. Artyomov, Alexey Sergushichev. Fast gene set enrichment analysis. Preprint at *bioRxiv* <https://doi.org/10.1101/060012> (2021).
93. Li, T. et al. TIMER2.0 for analysis of tumor-infiltrating immune cells. *Nucleic Acids Res* **48**, W509–W514 (2020).

Acknowledgements

We thank the EMBL Proteomics Core Facility and NorSeq Sequencing Core for proteomics and RNA-seq analysis, respectively. We thank Mehmet Ilyas Cosacak for his input on the scRNA-seq data analysis. FS was funded by the Norwegian Research Council (303353), Norwegian Cancer Society (247110), Helse Sør-Øst and Anders Jahre fund (102583101, 10000). MLK was funded by the Norwegian Research Council, Helse Sør-Øst, and the University of Oslo through the Center for Molecular Medicine Norway (187615), the Norwegian Research Council (313932), and the Norwegian Cancer Society (214871). MD, HZO, and SHYK were funded by a TerryFox New Frontiers Program Project Grant (1109-UBC GRO26025). MKT was funded by the Danish Cancer Society (311-A18039).

Author contributions

B.U. and F.S. conceived the study, designed the experiments, and wrote the manuscript. F.S. supervised the study. B.U. performed the experiments with the supervision of F.S. Except for scRNA-seq analysis, O.F.K. performed all the other RNA-seq analyses and also generated ectopic XBP1s expressing cell lines. Y.J. and O.F.K. helped with animal experiments. D.O. and M.L.K. analyzed the scRNA-seq data. W.K., M.P., S.H.Y.K., H.Z.O., and M.D. conducted and analyzed IHC analysis of PCa patient samples. M.K.T. performed orthotopic PCa model experiment and obtained the MRI images with the help of M.V. J.B.P. provided critical reagents. All authors revised the manuscript.

Competing interests

JB.P. is employee and shareholder of Fosun Orinove. The remaining authors declare no competing interests.

Additional information

Supplementary information The online version contains supplementary material available at <https://doi.org/10.1038/s41467-024-53039-1>.

Correspondence and requests for materials should be addressed to Fahri Saatcioglu.

Peer review information *Nature Communications* thanks Eric Chevet, John Lee and the other, anonymous, reviewer(s) for their contribution to the peer review of this work. A peer review file is available.

Reprints and permissions information is available at <http://www.nature.com/reprints>

Publisher's note Springer Nature remains neutral with regard to jurisdictional claims in published maps and institutional affiliations.

Open Access This article is licensed under a Creative Commons Attribution-NonCommercial-NoDerivatives 4.0 International License, which permits any non-commercial use, sharing, distribution and reproduction in any medium or format, as long as you give appropriate credit to the original author(s) and the source, provide a link to the Creative Commons licence, and indicate if you modified the licensed material. You do not have permission under this licence to share adapted material derived from this article or parts of it. The images or other third party material in this article are included in the article's Creative Commons licence, unless indicated otherwise in a credit line to the material. If material is not included in the article's Creative Commons licence and your intended use is not permitted by statutory regulation or exceeds the permitted use, you will need to obtain permission directly from the copyright holder. To view a copy of this licence, visit <http://creativecommons.org/licenses/by-nc-nd/4.0/>.

© The Author(s) 2024